

# CompMarkGS: Robust Watermarking for Compressed 3D Gaussian Splatting

Sumin In<sup>1</sup> Youngdong Jang<sup>1</sup> Utae Jeong<sup>1</sup>  
MinHyuk Jang<sup>1</sup> Hyeongcheol Park<sup>1</sup> Eunbyung Park<sup>2</sup> Sangpil Kim<sup>1\*</sup>

<sup>1</sup> Korea University <sup>2</sup> Yonsei University

## Abstract

3D Gaussian Splatting (3DGS) is increasingly adopted in various academic and commercial applications due to its real-time and high-quality rendering capabilities, emphasizing the growing need for copyright protection technologies for 3DGS. However, the large model size of 3DGS requires developing efficient compression techniques. This highlights the necessity of an integrated framework that addresses copyright protection and data compression for 3D content. Nevertheless, existing 3DGS watermarking methods significantly degrade watermark performance under 3DGS compression methods, particularly quantization-based approaches that achieve superior compression performance. To ensure reliable watermark detection under compression, we propose a compression-tolerant anchor-based 3DGS watermarking, which preserves watermark integrity and rendering quality. This is achieved by introducing *anchor-based 3DGS watermarking*. We embed the watermark into the anchor attributes, particularly the anchor feature, to enhance security and rendering quality. We also propose a *quantization distortion layer* that injects quantization noise during training, preserving the watermark after quantization-based compression. Moreover, we employ a *frequency-aware anchor growing strategy* that improves rendering quality and watermark performance by effectively identifying Gaussians in high-frequency regions. Extensive experiments demonstrate that our proposed method preserves the watermark even under compression and maintains high rendering quality.

## 1 Introduction

3D Gaussian Splatting (3DGS) [18] has recently emerged as an impactful method for novel view synthesis, offering real-time and photorealistic rendering capabilities. Since its introduction, 3DGS has undergone rapid advancements in the field of image-based 3D reconstruction [4, 23, 49], attracting significant attention from academia and industry. One drawback of 3DGS is that it is composed of a vast number of 3D Gaussians, requiring substantial storage space. This limitation has motivated the development of 3DGS compression techniques to reduce storage requirements and facilitate efficient transmission of 3DGS models.

In parallel, its growing commercial adoption in areas such as digital twin construction and AR/VR applications has raised critical concerns regarding the copyright protection of trained 3DGS models, which has led to increased research interest in 3DGS watermarking. However, to the best of our knowledge, no prior work has jointly tackled model compression and embedding watermarks for 3DGS models. In this paper, we propose the first 3DGS framework that jointly performs watermark embedding and compression, which can be used for ownership verification even after compression, as shown in Fig.1.

---

\*Corresponding Author

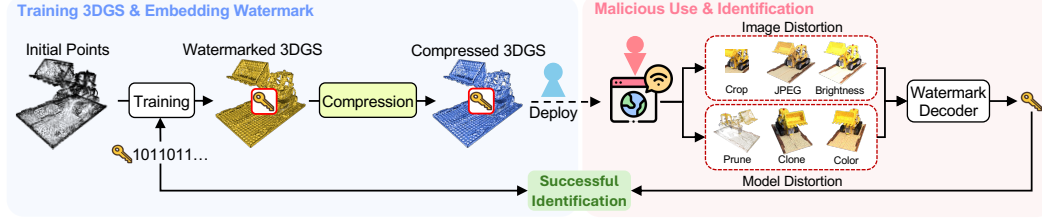


Figure 1: Application scenario of CompMarkGS. Owners embed the watermark into a 3DGS asset using our proposed method, then compress and distribute the model across various digital environments. The owner can extract the hidden message to verify ownership even if an unauthorized user alters the distributed model or its rendered images.

Existing 3DGS watermarking methods [8, 12, 13, 15, 35] embed watermarks by directly modifying Gaussian attributes, which makes the watermark vulnerable to loss when those attributes are altered during compression. In particular, quantization-based compression shifts the distribution of model parameters during the compression process, severely degrading watermark performance. As a result, existing methods fail to provide adequate copyright protection for compressed 3DGS models.

To handle this problem, we propose CompMarkGS, an anchor-based 3DGS watermarking strategy. Our method leverages the anchor-based 3DGS architecture, which dynamically predicts Gaussian attributes from anchor points via multiple implicit MLPs. This implicit representation makes it extremely difficult for an adversary to detect the presence of a watermark by directly analyzing the point cloud or Gaussian attributes. We seamlessly integrate the watermark by embedding a learnable watermark feature into the anchor feature, which is one of the anchor attributes, without altering the original model architecture. Unlike prior 3DGS watermarking methods that consider only image-domain distortions, we apply a quantization distortion layer during training to inject quantization noise into the watermark-embedded anchor attributes. By doing so, the embedded watermark learns to adapt to quantization-based compression. As a result, our model preserves watermark integrity through the compression process while maintaining high rendering quality.

To further improve rendering quality, we introduce a frequency-aware anchor growing strategy. Specifically, we identify high-frequency regions in the rendered image, map them to Gaussian coordinates, and selectively apply anchor growing in those regions. This strategy improves both rendering quality and the bit accuracy of the embedded watermark.

Furthermore, we design a HSV loss to address color artifacts that occur when embedding the watermark. To identify the artifacts, we construct a binary mask on the RGB channels by analyzing the hue (H), saturation (S), and value (V) components of the rendered images. This mask guides the loss computation by focusing regions with noticeable color artifacts, improving rendering quality.

Our extensive experiments on the Blender [29], LLFF [28], and Mip-NeRF 360 [3] datasets show that CompMarkGS preserves watermark integrity and rendering quality more effectively both before and after compression. Each component of our framework—anchor-based 3DGS watermarking, the quantization distortion layer, and the frequency-aware anchor growing strategy—independently enhances watermark fidelity while preserving rendering quality, even under compression and various watermarking attacks. Furthermore, our method outperforms state-of-the-art approaches across various watermark message lengths. Our main contributions are as follows:

- We propose CompMarkGS, a compression-tolerant anchor-based watermarking framework for 3DGS that embeds a learnable watermark embedding feature into anchor features, preserving the model structure and ensuring high rendering quality and bit accuracy.
- We introduce a quantization distortion layer that injects quantization noise during training, enabling 3DGS watermarking to remain robust against quantization-based compression while maintaining high rendering quality.
- We propose a frequency-aware anchor growing strategy that selectively expands anchors in high-frequency regions, which enhances both rendering quality and watermark bit accuracy, and a HSV loss that mitigates color artifacts to further improve rendering quality.

## 2 Related Works

**3D Gaussian Splatting representation.** 3D Gaussian Splatting (3DGS) [18] is an innovative technique for 3D representation that employs explicit primitives to model 3D worlds. It renders images by projecting these primitives into arbitrary viewpoints and seamlessly blending pixel colors via an  $\alpha$ -blender, achieving high-quality results while substantially accelerating real-time rendering. Thanks to these advantages, 3DGS has been widely adopted across various research areas, including avatars [1, 5, 32, 47], dynamic scenes [22, 42, 45, 57], and 3D generation [36, 44, 46, 54]. Recently, Scaffold-GS [25] has advanced the 3DGS framework by introducing anchor points to construct a hierarchical 3D representation. Anchor-based methods [21, 33, 40] effectively minimize redundant Gaussians, enhancing rendering quality and increasing robustness against view changes. This representation approach is promising for 3DGS compression optimization, as it reduces parameter counts while maintaining high-quality rendering.

**3D Gaussian Splatting compression.** To achieve high-quality rendering images, 3DGS [18] generates a considerable number of Gaussians, leading to significant storage overhead. To address the storage overhead, vector quantization methods [9, 20, 30, 43] have been widely explored. These methods prune Gaussians with minimal impact on rendering quality and use codebooks to encode the attributes of Gaussians compactly. More recently, anchor-based representations have gained significant attention in 3DGS [7, 25, 39]. Compression methods [6, 7, 39, 48] that leverage the structural relationships between anchors have shown superior performance. For example, HAC [7] reduces spatial redundancies among anchors by utilizing hash grids for parameter quantization and enabling entropy modeling. ContextGS [39] introduces a unified compression framework with a factorized prior, enabling entropy modeling of anchor features while leveraging hierarchical anchor relations to reduce redundancy among anchors. CAT-3DGS [48] projects Gaussian primitives onto PCA-aligned triplanes and applies spatial autoregressive coding to capture spatial correlations, thereby enhancing entropy coding efficiency. Given their compression efficiency, anchor-based representations are especially advantageous for real-world applications.

**Digital watermarking.** Digital watermarking has long been studied to protect the copyright of digital assets. Early approaches embed information in the pixel domain [38, 41] or the frequency domain [2, 19, 31, 37]. Driven by advances in deep learning, encoder-decoder-based methods [16, 26, 34, 56] were proposed, demonstrating competitive robustness against a variety of distortions compared to traditional techniques. Recently, efforts have extended watermarking to protect 3D models and their rendered content [53, 55]. In particular, in radiance field model watermarking, methods have been proposed to embed watermarks by leveraging the implicit neural representation (INR) of NeRF [29]. CopyRNeRF [27] is the first digital watermarking method for implicit NeRF, introducing a watermarked color representation. WaterF [14] is a plug-and-play method compatible with all radiance field representations, leveraging the frequency domain to achieve robust watermarking. With the advent of 3DGS [18], various watermarking methods have been proposed. GS-Hider [51] was the first to introduce steganography for 3DGS, and SecureGS [52] proposes an anchor-based steganographic framework. GaussianMarker [13] embeds the watermark by estimating the uncertainties of Gaussians and incorporating watermark-specific Gaussians into the existing model based on these uncertainties. 3D-GSW [15] achieves watermark embedding by selectively pruning Gaussians with minimal impact on rendering quality. GuardSplat [8] introduces an SH-aware message-embedding mechanism. However, model compression often leads to watermark loss, and robust watermarking methods against compression remain underexplored. Therefore, our work integrates 3DGS training with watermark embedding, ensuring robustness against degradations introduced by model compression.

## 3 Preliminaries

**Scaffold-GS.** Scaffold-GS [25] clusters adjacent Gaussians using anchor points, reducing redundancy. Initial anchor points are placed at voxel centers, and the attributes for each anchor consist of an anchor feature  $f \in \mathbb{R}^d$ , scaling factor  $l \in \mathbb{R}^3$ , and  $K$  learnable offsets  $O \in \mathbb{R}^{K \times 3}$ , where  $K$  is the number of Gaussians. Visible anchor points within the viewing frustum generate  $K$  Gaussians, with their positions computed as follows:

$$\mu_k = x_a + O_k \odot l, \quad (1)$$

where  $x_a \in \mathbb{R}^3$  is the anchor point position,  $O_k \in \mathbb{R}^3$  denotes the  $k$ -th offset vector,  $\mu_k$  is the generated  $k$ -th Gaussian position, and  $\odot$  represents the element-wise product. The Gaussian attributes

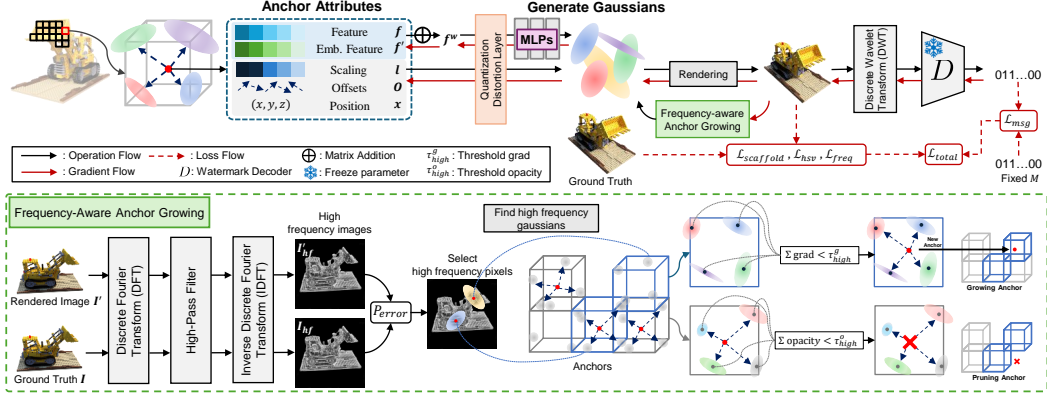


Figure 2: Overview of CompMarkGS. We obtain the watermarked anchor feature  $f^w$  by adding the watermark embedding feature  $f'$  to the anchor feature  $f$ . Quantized watermarked anchor feature from the quantization distortion layer are fed into individual MLPs to predict Gaussian attributes. We input the rendered image’s low-frequency band extracted via DWT into a pre-trained decoder to extract the watermark. Frequency-aware anchor growing strategy identifies Gaussians in high-frequency regions to introduce additional anchors, while an HSV loss  $\mathcal{L}_{hsv}$  and a frequency loss  $\mathcal{L}_{freq}$  further enhance rendering quality. Finally, the entire model is optimized using a total loss  $\mathcal{L}_{total}$ .

opacity  $\alpha_i$ , color  $c_i$ , quaternion  $q_i$  and scale  $s_i$  are predicted using separate MLPs:

$$\{\alpha_i, c_i, q_i, s_i\}_{i=1}^K = \text{MLP}(f, \delta_{av}, \vec{d}_{av}), \quad (2)$$

where  $\delta_{av} = \|x_a - x_v\|_2$  and  $\vec{d}_{av} = \frac{x_a - x_v}{\|x_a - x_v\|_2}$  denote the relative distance and viewing direction between the camera ( $x_v$ ) and the anchor ( $x_a$ ) positions.

## 4 Method

### 4.1 Anchor-based 3DGS watermarking

Anchor-based 3DGS [25], enhances the security of embedded watermarks by hiding explicit Gaussian attributes behind anchor features processed by implicit MLPs. This property of anchor-based 3DGS makes it more difficult for attackers to directly manipulate embedded watermarks and Gaussian attributes. Moreover, the anchor feature  $f$  influences the rendering quality indirectly through the MLPs rather than directly controlling Gaussian attributes. On the other hand, attributes like the position, scaling factor  $l$ , and offsets  $O$  directly determine Gaussian attributes, and modifying them leads to visible distortions in the rendered images.

To ensure rendering quality, we embed the watermark into the anchor feature, introducing a learnable watermark embedding feature  $f' \in \mathbb{R}^d$  of the same dimensionality as the anchor feature  $f \in \mathbb{R}^d$ . The resulting watermarked anchor feature  $f^w$  is defined as follows:

$$f^w = f + \tanh(f'), \quad \text{where } f, f' \in \mathbb{R}^d, \quad (3)$$

where  $\tanh(\cdot)$  represents the element-wise hyperbolic tangent function. To prevent the watermark embedding feature from growing excessively, we use  $\tanh(\cdot)$  to constrain its values to the range of  $[-1, 1]$  before adding it to the anchor feature.

### 4.2 Robustness to quantization-based compression

We aim to ensure that the watermarked model retains its watermark information after the model compression. Since many compression methods rely on quantization, we incorporate a quantization distortion layer to improve watermark robustness during compression. Specifically, we leverage the quantization technique used in anchor-based 3DGS compression [7] to inject quantization noise into the watermarked anchor feature  $f^w$  during training. This approach prevents the loss of watermark information during subsequent quantization-based compression. The quantized watermarked anchor



feature  $\tilde{f}_i^w$  for the  $i$ -th anchor is defined as follows:

$$\tilde{f}_i^w = f_i^w + \mathcal{U}\left(-\frac{1}{2}, \frac{1}{2}\right) \cdot q_i, \quad \text{where} \quad q_i = Q_0 \cdot \left(1 + \tanh(r_i)\right), \quad r_i = \text{MLP}_q(f_i^w), \quad (4)$$

where  $q_i \in \mathbb{R}$  denotes the quantization scale restricted to  $[0, 2Q_0]$ , and  $r_i \in \mathbb{R}$  is the refinement output from an  $\text{MLP}_q$  that takes  $f_i^w$  as input, used to adjust the initial quantization scale  $Q_0$ . Thus, by scaling a randomly generated  $d$ -dimensional noise vector from a uniform distribution over  $[-\frac{1}{2}, \frac{1}{2}]$  by  $q_i$  and adding it to the watermarked anchor feature  $f_i^w$ , we simulate the rounding error caused by quantization, thus reflecting the effects of quantization during training.

### 4.3 Frequency-aware anchor growing

We apply a Discrete Wavelet Transform (DWT) to the rendered image and feed its low-frequency Low-Low ( $LL$ ) subband,  $I_{LL}$ , into the pre-trained HiDDeN [56] decoder  $D$  to extract the watermark message  $M'$ , which is defined as follows:

$$M' = D(I_{LL}). \quad (5)$$

However, since the low-frequency band encodes the global structure of the image, embedding a watermark in this region may induce subtle deformations of the overall structure, resulting in blurred boundaries or slight texture distortions. The conventional anchor-growing strategy generates new anchors in voxels where Gaussian gradients are large during training, distributing anchors uniformly across the scene without regard to specific regions, which can cause loss of fine detail.

To address this, we propose a frequency-aware anchor growing strategy that selectively grows anchors in high-frequency regions rich in detail, such as textures. As shown in Fig. 2, we first transform the rendered image  $I'$  and the ground truth image  $I$  into the frequency domain via the Discrete Fourier Transform (DFT). We then apply a high-pass filter to isolate the high-frequency components and reconstruct the high-frequency images  $I'_{hf}$  and  $I_{hf}$  by applying the Inverse Discrete Fourier Transform (IDFT). To generate a binary mask that selects pixels in the high-frequency region, we define the pixel-wise SSIM loss  $P_{error}$  as follows:

$$P_{error}(p) = 1 - \text{SSIM}(I_{hf}(p), I'_{hf}(p)), \quad (6)$$

where  $p$  denotes a pixel coordinate in the image,  $I'_{hf}(p)$  denotes the pixel value in the high-frequency region of the rendered image, and  $I_{hf}(p)$  corresponds to a pixel value in the high-frequency region of the ground truth image. After computing the median of all pixel-wise SSIM losses, denoted as  $\tilde{P}_{error}$ , we select pixels within the range  $[\tilde{P}_{error} - \epsilon, \tilde{P}_{error} + \epsilon]$  to create a binary mask, which is then used to extract the 2D coordinates of pixels in the high-frequency region. Subsequently, each 3D Gaussian point is projected onto the 2D image plane, and its continuous coordinates are rounded to obtain integer pixel-level coordinates. We match the 2D Gaussian coordinates with the high-frequency pixel coordinates, generating a boolean mask  $F_{mask}$  that identifies anchors located in the high-frequency region. The Gaussians selected by  $F_{mask}$  are considered active for the anchor growing process.

### 4.4 Objective function

**HSV Loss.** We incorporate the HSV loss  $\mathcal{L}_{hsv}$  term to minimize color artifacts during watermark embedding. Previous studies [13, 14, 15] typically computed image loss in the RGB space to improve rendering quality. However, since the RGB space calculates loss based on independent pixel-level color information, it does not accurately reflect the human visual system. Therefore, we compute image loss in the HSV space, which represents colors in a manner more similar to the human visual system. First, we construct binary masks based on hue ranges for each color to localize color artifacts. Binary mask is defined as follows:

$$M_c(p) = \begin{cases} 1, & \text{if Hue}(p) \in H_c \\ 0, & \text{otherwise} \end{cases}, \quad (7)$$

where  $H_c$  denotes the hue range corresponding to color  $c \in \mathcal{C}$ , with  $\mathcal{C} = \{R, G, B\}$ .  $R$ ,  $G$ , and  $B$  represent the red, green, and blue color channels, respectively.

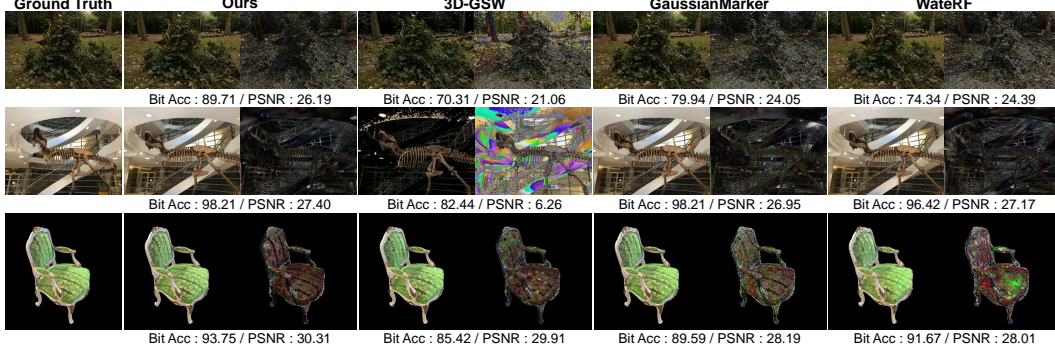


Figure 3: Qualitative comparison of rendering quality after compression between our method and baselines. For each method, the rendered image (left) and the difference map (right) are shown. Note that the difference maps are magnified five times. This result is based on 48-bit messages.

Then, HSV loss  $\mathcal{L}_{hsv}$  is computed as the mean squared error (MSE) between the pixel value of rendered image  $I(p)$  and the ground truth  $I_{gt}(p)$  over the pixels in the set  $\Omega$  where  $M_c(p) = 1$ :

$$\mathcal{L}_{hsv} = \frac{1}{|\mathcal{C}||\Omega|} \sum_{c \in \mathcal{C}} \sum_{p \in \Omega} \|M_c(p) \cdot (I(p) - I_{gt}(p))\|^2. \quad (8)$$

The overall color loss is defined as the average of the losses for each target color in the set  $\mathcal{C}$ .

**Watermark message loss.** As described in Sec.4.3, we use the pre-trained HiDDeN [56] decoder to produce the watermark message  $M'$ , and the watermark message loss  $\mathcal{L}_{msg}$  is defined as a binary cross entropy (BCE) loss:

$$\mathcal{L}_{msg} = - \sum_{i=1}^L \left[ M_i \log(\sigma(M'_i)) + (1 - M_i) \log(1 - \sigma(M'_i)) \right], \quad (9)$$

where  $M \in \{0, 1\}^L$  is the ground truth message, and a sigmoid function  $\sigma$  constrains  $M'$  to  $[0, 1]$ .

**Total Loss.** Additionally, we employ frequency loss  $\mathcal{L}_{freq}$  to reduce high-frequency distortions during watermark embedding. The overall training loss for our method is given by:

$$\mathcal{L}_{total} = \lambda_{img}(\mathcal{L}_{scaffold} + \lambda_{hsv}\mathcal{L}_{hsv} + \lambda_{freq}\mathcal{L}_{freq}) + \lambda_{msg}\mathcal{L}_{msg}, \quad (10)$$

where  $\mathcal{L}_{freq} = \frac{1}{|\mathcal{P}|} \sum_{p \in \mathcal{P}} P_{error}(p)$ , as the mean of all pixel-wise SSIM losses.  $\mathcal{L}_{scaffold}$  represents the reconstruction loss defined in Scaffold-GS [25], which consists of one scale regularization and two rendering fidelity terms.

## 5 Experiments

### 5.1 Experimental Setting

**Datasets.** Following previous works [13, 15], we evaluate our method using the Blender [29], LLFF [28], and Mip-NeRF 360 [3] datasets. We use all 25 scenes: 8 synthetic bounded scenes from the Blender dataset, 8 forward-facing real-world scenes from the LLFF dataset, and 9 bounded real-world scenes from the Mip-NeRF 360 dataset. We assess performance using 200 test images from the Blender dataset. For the LLFF and Mip-NeRF 360 datasets, we adopt the same data split strategy as Mip-NeRF 360.

**Implementation details.** Our method trains end-to-end on a single A6000 GPU. We conduct experiments for watermark bit-lengths of 32, 48, and 64, focusing on the 48-bit case, where we evaluate both before and after compression performance. For the decoder, we use a pre-trained HiDDeN [56] decoder for each bit-length and keep its parameters fixed during watermark training. We use the following parameters:  $\lambda_{img} = 10$ ,  $\lambda_{hsv} = 0.6$ ,  $\lambda_{freq} = 0.1$ ,  $\lambda_{msg} = 0.45$ . For the quantization scale and anchor growing range in high-frequency regions, we set  $Q_0 = 1$ ,  $\epsilon = 0.3$ .

Table 1: Quantitative comparison of before (left) and after (right) compression bit accuracy and rendering quality. Evaluations are performed using a 48-bit setting, averaged over the Blender, LLFF, and Mip-NeRF 360 datasets. Baselines are tested within an anchor-based 3DGS framework with HAC and ContextGS compression. The best results are in **bold**.

Methods	Bit Accuracy(%) $\uparrow$	PSNR $\uparrow$	SSIM $\uparrow$	LPIPS $\downarrow$	Size(MB) $\downarrow$
HAC [7] + WaterRF [14]	91.02 / 54.40	27.36 / 13.63	0.850 / 0.457	0.174 / 0.574	207.72 / 13.66
HAC [7] + GaussianMarker [13]	92.00 / 58.34	27.05 / 13.54	0.840 / 0.460	0.193 / 0.571	341.30 / 24.33
HAC [7] + 3D-GSW [15]	90.96 / 53.48	19.57 / 13.13	0.628 / 0.439	0.295 / 0.572	<b>173.64</b> / 12.93
HAC [7] + CompMarkGS	<b>95.95 / 95.92</b>	<b>27.68 / 27.65</b>	<b>0.856 / 0.852</b>	<b>0.171 / 0.177</b>	208.96 / <b>12.23</b>
ContextGS [39] + WaterRF [14]	92.01 / 90.36	26.64 / 26.47	0.843 / 0.832	0.183 / 0.185	219.48 / 9.88
ContextGS [39] + GaussianMarker [13]	91.24 / 87.95	26.89 / 26.54	0.839 / 0.827	0.195 / 0.200	342.38 / 17.86
ContextGS [39] + 3D-GSW [15]	88.28 / 79.75	19.50 / 19.83	0.627 / 0.617	0.294 / 0.299	177.19 / 9.24
ContextGS [39] + CompMarkGS	<b>94.36 / 94.03</b>	<b>27.60 / 27.55</b>	<b>0.845 / 0.844</b>	<b>0.172 / 0.173</b>	<b>73.39 / 5.72</b>

Table 2: Robustness to image distortion before (left) and after (right) compression. Evaluations are performed using a 48-bit setting, averaged over the Blender, LLFF, and Mip-NeRF 360 datasets. Baselines are tested within an anchor-based 3DGS framework with HAC and ContextGS compression. The best results are in **bold**.

Methods	Bit Accuracy(%) $\uparrow$						
	No Distortion	Gaussian Noise ( $\sigma = 0.1$ )	Rotation ( $\pm\pi/6$ )	Scaling (75%)	Gaussian Blur ( $\sigma = 0.1$ )	Crop (40%)	JPEG Compression (50% quality)
HAC [7] + WaterRF [14]	91.02 / 54.40	89.75 / 55.90	84.92 / 56.16	86.17 / 55.38	89.33 / 56.34	87.00 / 55.30	84.00 / 57.47
HAC [7] + GaussianMarker [13]	92.00 / 58.34	59.08 / 58.33	58.75 / 58.33	58.33 / 58.33	59.08 / 58.33	61.42 / 58.17	58.25 / 58.33
HAC [7] + 3D-GSW [15]	90.96 / 53.48	89.50 / 52.50	86.67 / 52.25	86.42 / 52.08	86.67 / 52.25	86.92 / 52.50	83.83 / 53.25
HAC [7] + CompMarkGS	<b>95.95 / 95.92</b>	<b>96.00 / 95.50</b>	<b>92.25 / 92.08</b>	<b>91.83 / 91.67</b>	<b>95.83 / 95.58</b>	<b>90.67 / 90.83</b>	<b>87.75 / 88.83</b>
ContextGS [39] + WaterRF [14]	92.01 / 90.36	92.25 / 91.50	88.75 / 88.00	89.58 / 88.83	92.75 / 91.50	89.50 / 88.25	<b>86.41</b> / 84.58
ContextGS [39] + GaussianMarker [13]	91.24 / 87.95	59.08 / 58.92	59.00 / 58.75	58.25 / 58.17	59.17 / 58.92	61.08 / 60.67	58.25 / 58.25
ContextGS [39] + 3D-GSW [15]	88.28 / 79.25	87.92 / 80.67	85.08 / 78.75	84.42 / 77.08	88.00 / 81.42	84.33 / 78.50	81.58 / 72.58
ContextGS [39] + CompMarkGS	<b>94.36 / 94.03</b>	<b>93.04 / 92.98</b>	<b>90.17 / 90.33</b>	<b>90.46 / 90.06</b>	<b>92.96 / 92.81</b>	<b>89.63 / 89.29</b>	85.21 / <b>85.31</b>

**Baselines.** We perform message extraction experiments before and after compression using anchor-based 3DGS with quantization-based compression, validating the effectiveness of our method. For comparison, we evaluate against the following three baselines: 1) WaterRF [14]: Embedding watermark into NeRF [29] via frequency-domain (DWT) techniques; 2) GaussianMarker [13]: Integrating watermark-specific Gaussians into the 3D Gaussian Splatting (3DGS) [18] based on per-Gaussian uncertainty estimates; 3) 3D-GSW [15]: Pruning only those Gaussians whose removal minimally impacts rendering quality, embedding the watermark into the remaining primitives. All three baselines originally designed for NeRF or 3DGS were adapted to the anchor-based 3DGS framework for our experiments. We compare their performance before and after compression using two quantization-based compression schemes: HAC [7] and ContextGS [39].

**Evaluation.** We evaluate the watermark performance of CompMarkGS and the baselines according to three aspects: 1) Fidelity: We measure PSNR, SSIM, and LPIPS [50] to assess the rendering quality of watermarked models before and after compression by comparing rendered images to the original images. 2) Robustness: We evaluate bit accuracy under various distortions before and after compression. We evaluate performance under distortions for rendered images, including Gaussian noise, rotation, scaling, Gaussian blur, cropping, and JPEG compression. We assess robustness against Gaussian noise, cloning, and pruning attacks for watermarked models. 3) Capacity: We measure bit accuracy for 32, 48, and 64-bit message lengths.

## 5.2 Experimental results

**Fidelity of before and after compression.** We compare rendering quality and bit accuracy before and after compression against baseline methods. The compression technique compresses anchor-based 3DGS models using quantization and entropy encoding. As shown in Tab. I, our proposed method exhibits strong robustness to compression. While some baselines achieve higher rendering quality before compression, conventional methods without the quantization distortion layer suffer significant watermark and scene information degradation after compression (see Fig.3). In particular, the HAC [7]-based method shows the most significant performance drop, as existing approaches fine-tune without accounting for both the quantization process and the interpolation required for HAC entropy encoding.

Table 3: Robustness to model distortion. Based on 48-bit, results are averaged over three datasets with both HAC&ContextGS before (left) and after (right) compression.

Methods	Bit Accuracy(%) $\uparrow$			
	No Distortion	Gaussian Noise ( $\sigma=0.005$ )	Clone (50%)	Prune (20%)
WateRF [14]	91.52 / 72.38	81.70 / 63.27	90.23 / 67.45	87.81 / 66.25
GaussianMarker [13]	91.62 / 73.15	73.01 / 65.07	89.83 / 72.17	87.43 / 85.73
3D-GSW [15]	89.62 / 62.89	78.56 / 57.72	88.26 / 62.14	84.84 / 59.76
CompMarkGS	<b>95.16 / 94.98</b>	<b>84.58 / 80.10</b>	<b>94.35 / 94.16</b>	<b>93.53 / 93.42</b>

Table 4: Comparison of bit accuracy for our method and baselines at 32, 48, and 64-bit. Results are averaged over three datasets with both HAC&ContextGS before compression.

Methods	Bit Accuracy(%) $\uparrow$		
	32 bits	48 bits	64 bits
WateRF [14]	92.46	91.52	88.21
GaussianMarker [13]	95.07	91.62	79.81
3D-GSW [15]	93.00	89.62	86.31
CompMarkGS	<b>96.52</b>	<b>95.16</b>	<b>91.29</b>

Similarly, the ContextGS [39]-based method experiences a decline in bit accuracy and rendering quality. Moreover, 3D-GSW [15], which performs pruning based on rendering contributions before watermark training, removes both anchors and their associated Gaussians, significantly degrading rendering quality. These results confirm that our proposed watermarking technique is more suited to model compression than existing methods.

**Robustness for the image distortion.** We evaluate the robustness of our method against the loss of the embedded watermark when the rendered image is subjected to various distortions. Specifically, we apply six different post-processing techniques to the rendered images: Gaussian noise ( $\sigma = 0.1$ ), rotation (random selection within  $\pm\pi/6$ ), scaling (75% of the original), Gaussian blur ( $\sigma = 0.1$ ), crop (40% of the original), and JPEG compression (50% of the original). As shown in Tab.2, we assess the watermark bit accuracy after post-processing and observe a decrease in bit accuracy, but the performance degradation is relatively minor compared to the baselines. These results demonstrate that our proposed watermark embedding technique is robust against image distortion.

**Robustness for the model distortion.** We evaluate the robustness of our method against direct manipulation of the trained model, which may alter the embedded watermark information. We conduct three model distortion experiments: Gaussian noise ( $\sigma = 0.005$ ), clone (randomly clone 50%), and prune (randomly remove 20%). Gaussian noise is applied by adding noise with standard deviation  $\sigma$  to the model parameters, while pruning and cloning are performed by randomly removing or duplicating anchors, respectively. As shown in Tab.3, we evaluate bit accuracy under various model attacks, and our method demonstrates superior robustness compared to existing approaches. These results confirm that our proposed technique reliably preserves the embedded watermark even when the model is subjected to distortion attacks.

**Capacity.** The number of embedded watermark bits in the rendered image represents a trade-off between image quality and bit accuracy. We conduct experiments using 32, 48, and 64-bit. As shown in Tab.4, increasing the number of embedded watermark bits results in a degradation of image quality and bit accuracy. However, our proposed method shows that even with a larger number of bits, the performance degradation is reduced compared to others.

### 5.3 Ablation Study

**Anchor-based 3DGS watermark embedding.** We embed the watermark into different anchor attributes (position, scaling, and offsets) and compare the resulting rendering quality and bit accuracy. As discussed in the previous section (Sec.4.1), since the watermark embedding feature shares the same dimensions as the anchor feature, we ensure consistency across all attributes before embedding. As shown in Fig.4 and Tab.5, embedding the watermark into anchor attributes other than the anchor feature leads to degraded rendering quality compared to embedding it into the anchor feature.

In particular, the anchor position and the scaling lead to significant quality degradation because these attributes directly adjust the Gaussian pose and shape. These results demonstrate that our method seamlessly integrates the watermark into the scene’s features without significantly degrading the scene information.

**Quantization distortion layer.** We evaluate the effectiveness of the quantization distortion layer (QDL) during the quantization process by comparing rendering quality and bit accuracy before and after compression, with and without QDL. We use HAC [7], a quantization-based 3DGS compression method. Tab.6 reports the results after compression for HAC, showing that performance without QDL is noticeably worse than with QDL. Without QDL during training, the anchor attributes carrying the watermark fail to adapt to the quantization process, leading to information loss and reduced bit accuracy.

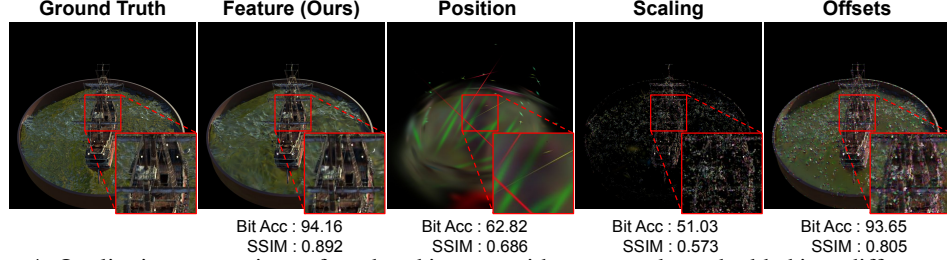


Figure 4: Qualitative comparison of rendered images with watermarks embedded into different anchor attributes. Rendered images are obtained with 48-bit watermark embedding.

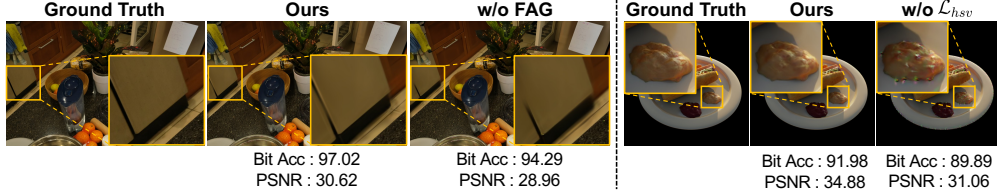


Figure 5: Qualitative comparison of rendering quality with full method (ours), without FAG (left), without  $\mathcal{L}_{hsv}$  (right). Rendered images are obtained with 48-bit watermark embedding.

Table 5: Ablation studies on watermark embedding into different anchor attributes. Results are reported for 48-bit watermarks and averaged over three datasets using HAC after compression.

Target Parameter	Bit Acc(%) $\uparrow$	PSNR $\uparrow$	SSIM $\uparrow$	LPIPS $\downarrow$
Position	67.91	12.05	0.625	0.350
Scaling	65.06	19.35	0.615	0.323
Offsets	94.88	24.61	0.792	0.226
Anchor Feature (Ours)	<b>95.92</b>	<b>27.65</b>	<b>0.852</b>	<b>0.177</b>

Table 6: Ablation studies on quantization distortion layer (QDL) and FAG. Based on 48-bit, results are averaged over three datasets with HAC after compression.

Methods	Bit Acc(%) $\uparrow$	PSNR $\uparrow$	SSIM $\uparrow$	LPIPS $\downarrow$
w/o QDL + w/ FAG	90.75	26.75	0.844	0.182
w/ QDL + w/o FAG	93.95	27.54	0.849	0.178
w/ QDL + w/ FAG	<b>95.92</b>	<b>27.65</b>	<b>0.852</b>	<b>0.177</b>

In contrast, applying QDL allows the anchor attributes to adapt to the quantization process during training, thereby minimizing information loss. These results demonstrate that the watermark embedded using QDL remains robust under quantization.

**Frequency-aware anchor growing and HSV loss.** To evaluate our proposed frequency-aware anchor growing (FAG) and HSV loss  $\mathcal{L}_{hsv}$  for mitigating distortion during watermark embedding, we compare performance with and without each component. As shown in Tab.6 and Fig.5, bit accuracy improves when FAG is enabled. This improvement arises because FAG selectively grows anchors in regions lacking detailed Gaussians, increasing the number of Gaussians available for watermark insertion. Additionally, rendering quality improves further than without HSV loss. Fig.5 also shows that HSV loss effectively removes color artifacts of rendered images. These results underscore the importance of both components in reducing watermark-induced distortions.

## 6 Conclusion

We propose CompMarkGS, a compression-robust watermarking method. By integrating a quantization distortion layer, we train the watermark to withstand quantization-based compression, and we introduce a learnable watermark embedding feature for anchor-based insertion, achieving both high security and high fidelity. Additionally, our frequency-aware anchor growing and HSV loss preserve high-quality rendering performance. To the best of our knowledge, CompMarkGS is the first compression-robust watermarking framework for 3DGS, making it well suited for protecting 3D assets on resource-constrained devices.

**Limitations and future works.** CompMarkGS requires a pre-trained decoder. However, since the decoder needs training only once per bit-length, subsequent usage is efficient without additional fine-tuning. We will extend our method beyond 3DGS compression and develop a lightweight watermarking approach for 3DGS.

## References

- [1] Rameen Abdal, Wang Yifan, Zifan Shi, Yinghao Xu, Ryan Po, Zhengfei Kuang, Qifeng Chen, Dit-Yan Yeung, and Gordon Wetzstein. Gaussian shell maps for efficient 3d human generation. In *Proceedings of the IEEE/CVF Conference on Computer Vision and Pattern Recognition*, pages 9441–9451, 2024.
- [2] Mauro Barni, Franco Bartolini, and Alessandro Piva. Improved wavelet-based watermarking through pixel-wise masking. *IEEE transactions on image processing*, 10(5):783–791, 2001.
- [3] Jonathan T Barron, Ben Mildenhall, Dor Verbin, Pratul P Srinivasan, and Peter Hedman. Mip-nerf 360: Unbounded anti-aliased neural radiance fields. In *Proceedings of the IEEE/CVF conference on computer vision and pattern recognition*, pages 5470–5479, 2022.
- [4] David Charatan, Sizhe Lester Li, Andrea Tagliasacchi, and Vincent Sitzmann. pixelsplat: 3d gaussian splats from image pairs for scalable generalizable 3d reconstruction. In *Proceedings of the IEEE/CVF conference on computer vision and pattern recognition*, pages 19457–19467, 2024.
- [5] Jianchuan Chen, Jingchuan Hu, Gaige Wang, Zhonghua Jiang, Tiansong Zhou, Zhiwen Chen, and Chengfei Lv. Taoavatar: Real-time lifelike full-body talking avatars for augmented reality via 3d gaussian splatting. *arXiv preprint arXiv:2503.17032*, 2025.
- [6] Yihang Chen, Mengyao Li, Qianyi Wu, Weiyao Lin, Mehrtash Harandi, and Jianfei Cai. PcgS: Progressive compression of 3d gaussian splatting. *arXiv preprint arXiv:2503.08511*, 2025.
- [7] Yihang Chen, Qianyi Wu, Weiyao Lin, Mehrtash Harandi, and Jianfei Cai. Hac: Hash-grid assisted context for 3d gaussian splatting compression. In *European Conference on Computer Vision*, pages 422–438. Springer, 2024.
- [8] Zixuan Chen, Guangcong Wang, Jiahao Zhu, Jianhuang Lai, and Xiaohua Xie. Guardsplat: Robust and efficient watermarking for 3d gaussian splatting. *arXiv preprint arXiv:2411.19895*, 2024.
- [9] Zhiwen Fan, Kevin Wang, Kairun Wen, Zehao Zhu, Dejia Xu, Zhangyang Wang, et al. Light-gaussian: Unbounded 3d gaussian compression with 15x reduction and 200+ fps. *Advances in neural information processing systems*, 37:140138–140158, 2025.
- [10] Pierre Fernandez, Guillaume Couairon, Hervé Jégou, Matthijs Douze, and Teddy Furon. The stable signature: Rooting watermarks in latent diffusion models. In *Proceedings of the IEEE/CVF International Conference on Computer Vision*, pages 22466–22477, 2023.
- [11] Rafael C Gonzalez. *Digital image processing*. Pearson education india, 2009.
- [12] Yijia Guo, Wenkai Huang, Yang Li, Gaolei Li, Hang Zhang, Liwen Hu, Jianhua Li, Tiejun Huang, and Lei Ma. Splats in splats: Embedding invisible 3d watermark within gaussian splatting. *arXiv preprint arXiv:2412.03121*, 2024.
- [13] Xiufeng Huang, Ruiqi Li, Yiu-ming Cheung, Ka Chun Cheung, Simon See, and Renjie Wan. Gaussianmarker: Uncertainty-aware copyright protection of 3d gaussian splatting. *Advances in Neural Information Processing Systems*, 37:33037–33060, 2025.
- [14] Youngdong Jang, Dong In Lee, MinHyuk Jang, Jong Wook Kim, Feng Yang, and Sangpil Kim. Waterf: Robust watermarks in radiance fields for protection of copyrights. In *Proceedings of the IEEE/CVF Conference on Computer Vision and Pattern Recognition*, pages 12087–12097, 2024.
- [15] Youngdong Jang, Hyunje Park, Feng Yang, Heeju Ko, Euijin Choo, and Sangpil Kim. 3d-gsw: 3d gaussian splatting for robust watermarking. In *Proceedings of the IEEE/CVF Conference on Computer Vision and Pattern Recognition*, 2025.
- [16] Zhengyuan Jiang, Jinghuai Zhang, and Neil Zhenqiang Gong. Evading watermark based detection of ai-generated content. In *Proceedings of the 2023 ACM SIGSAC Conference on Computer and Communications Security*, pages 1168–1181, 2023.

- [17] Lih-Jen Kau and Tien-Lin Lee. An hsv model-based approach for the sharpening of color images. In *2013 IEEE International Conference on Systems, Man, and Cybernetics*, pages 150–155. IEEE, 2013.
- [18] Bernhard Kerbl, Georgios Kopanas, Thomas Leimkühler, and George Drettakis. 3d gaussian splatting for real-time radiance field rendering. *ACM Transactions on Graphics*, 42(4):1–14, 2023.
- [19] Martin Kutter, Frederic D Jordan, and Frank Bossen. Digital signature of color images using amplitude modulation. In *Storage and Retrieval for Image and Video Databases V*, volume 3022, pages 518–526. SPIE, 1997.
- [20] Joo Chan Lee, Daniel Rho, Xiangyu Sun, Jong Hwan Ko, and Eunbyung Park. Compact 3d gaussian representation for radiance field. In *Proceedings of the IEEE/CVF Conference on Computer Vision and Pattern Recognition*, pages 21719–21728, 2024.
- [21] Yonghan Lee, Jaehoon Choi, Dongki Jung, Jaeseong Yun, Soohyun Ryu, Dinesh Manocha, and Suyong Yeon. Mode-gs: Monocular depth guided anchored 3d gaussian splatting for robust ground-view scene rendering. *arXiv preprint arXiv:2410.04646*, 2024.
- [22] Zhan Li, Zhang Chen, Zhong Li, and Yi Xu. Spacetime gaussian feature splatting for real-time dynamic view synthesis. In *Proceedings of the IEEE/CVF Conference on Computer Vision and Pattern Recognition*, pages 8508–8520, 2024.
- [23] Jiaqi Lin, Zhihao Li, Xiao Tang, Jianzhuang Liu, Shiyong Liu, Jiayue Liu, Yangdi Lu, Xiaofei Wu, Songcen Xu, Youliang Yan, et al. Vastgaussian: Vast 3d gaussians for large scene reconstruction. In *Proceedings of the IEEE/CVF Conference on Computer Vision and Pattern Recognition*, pages 5166–5175, 2024.
- [24] Tsung-Yi Lin, Michael Maire, Serge Belongie, James Hays, Pietro Perona, Deva Ramanan, Piotr Dollár, and C Lawrence Zitnick. Microsoft coco: Common objects in context. In *Computer vision–ECCV 2014: 13th European conference, zurich, Switzerland, September 6–12, 2014, proceedings, part v 13*, pages 740–755. Springer, 2014.
- [25] Tao Lu, Mulin Yu, Linning Xu, Yuanbo Xiangli, Limin Wang, Dahua Lin, and Bo Dai. Scaffold-gs: Structured 3d gaussians for view-adaptive rendering. In *Proceedings of the IEEE/CVF Conference on Computer Vision and Pattern Recognition*, pages 20654–20664, 2024.
- [26] Xiyang Luo, Ruohan Zhan, Huiwen Chang, Feng Yang, and Peyman Milanfar. Distortion agnostic deep watermarking. In *Proceedings of the IEEE/CVF conference on computer vision and pattern recognition*, pages 13548–13557, 2020.
- [27] Ziyuan Luo, Qing Guo, Ka Chun Cheung, Simon See, and Renjie Wan. Copyrnerf: Protecting the copyright of neural radiance fields. In *Proceedings of the IEEE/CVF international conference on computer vision*, pages 22401–22411, 2023.
- [28] Ben Mildenhall, Pratul P Srinivasan, Rodrigo Ortiz-Cayon, Nima Khademi Kalantari, Ravi Ramamoorthi, Ren Ng, and Abhishek Kar. Local light field fusion: Practical view synthesis with prescriptive sampling guidelines. *ACM Transactions on Graphics (ToG)*, 38(4):1–14, 2019.
- [29] Ben Mildenhall, Pratul P Srinivasan, Matthew Tancik, Jonathan T Barron, Ravi Ramamoorthi, and Ren Ng. Nerf: Representing scenes as neural radiance fields for view synthesis. *Communications of the ACM*, 65(1):99–106, 2021.
- [30] KL Navaneet, Kossar Pourahmadi Meibodi, Soroush Abbasi Koohpayegani, and Hamed Pirsiavash. Compgs: Smaller and faster gaussian splatting with vector quantization. In *European Conference on Computer Vision*, pages 330–349. Springer, 2024.
- [31] KA Navas, Mathews Cheriyan Ajay, M Lekshmi, Tampy S Archana, and M Sasikumar. Dwt-dct-svd based watermarking. In *2008 3rd international conference on communication systems software and middleware and workshops (COMSWARE’08)*, pages 271–274. IEEE, 2008.



- [32] Zhiyin Qian, Shaofei Wang, Marko Mihajlovic, Andreas Geiger, and Siyu Tang. 3dgs-avatar: Animatable avatars via deformable 3d gaussian splatting. In *Proceedings of the IEEE/CVF conference on computer vision and pattern recognition*, pages 5020–5030, 2024.
- [33] Kerui Ren, Lihan Jiang, Tao Lu, Mulin Yu, Linning Xu, Zhangkai Ni, and Bo Dai. Octree-gs: Towards consistent real-time rendering with lod-structured 3d gaussians. *arXiv preprint arXiv:2403.17898*, 2024.
- [34] Tom Sander, Pierre Fernandez, Alain Durmus, Teddy Furon, and Matthijs Douze. Watermark anything with localized messages. *arXiv preprint arXiv:2411.07231*, 2024.
- [35] Yuqi Tan, Xiang Liu, Shuzhao Xie, Bin Chen, Shu-Tao Xia, and Zhi Wang. Water-gs: Toward copyright protection for 3d gaussian splatting via universal watermarking. *arXiv preprint arXiv:2412.05695*, 2024.
- [36] Jiaxiang Tang, Jiawei Ren, Hang Zhou, Ziwei Liu, and Gang Zeng. Dreamgaussian: Generative gaussian splatting for efficient 3d content creation. *arXiv preprint arXiv:2309.16653*, 2023.
- [37] Matthieu Urvoy, Dalila Goudia, and Florent Autrusseau. Perceptual dft watermarking with improved detection and robustness to geometrical distortions. *IEEE Transactions on Information Forensics and Security*, 9(7):1108–1119, 2014.
- [38] Ron G Van Schyndel, Andrew Z Tirkel, and Charles F Osborne. A digital watermark. In *Proceedings of 1st international conference on image processing*, volume 2, pages 86–90. IEEE, 1994.
- [39] Yufei Wang, Zhihao Li, Lanqing Guo, Wenhan Yang, Alex C Kot, and Bihan Wen. Contextgs: Compact 3d gaussian splatting with anchor level context model. *arXiv preprint arXiv:2405.20721*, 2024.
- [40] Yuxin Wang, Qianyi Wu, Guofeng Zhang, and Dan Xu. Learning 3d geometry and feature consistent gaussian splatting for object removal. In *European Conference on Computer Vision*, pages 1–17. Springer, 2024.
- [41] Raymond B Wolfgang and Edward J Delp. A watermark for digital images. In *Proceedings of 3rd IEEE International Conference on Image Processing*, volume 3, pages 219–222. IEEE, 1996.
- [42] Guanjun Wu, Taoran Yi, Jiemin Fang, Lingxi Xie, Xiaopeng Zhang, Wei Wei, Wenyu Liu, Qi Tian, and Xinggang Wang. 4d gaussian splatting for real-time dynamic scene rendering. In *Proceedings of the IEEE/CVF conference on computer vision and pattern recognition*, pages 20310–20320, 2024.
- [43] Shuzhao Xie, Weixiang Zhang, Chen Tang, Yunpeng Bai, Rongwei Lu, Shijia Ge, and Zhi Wang. Mesongs: Post-training compression of 3d gaussians via efficient attribute transformation. In *European Conference on Computer Vision*, pages 434–452. Springer, 2024.
- [44] Tianyi Xie, Zeshun Zong, Yuxing Qiu, Xuan Li, Yutao Feng, Yin Yang, and Chenfanfu Jiang. Physgaussian: Physics-integrated 3d gaussians for generative dynamics. In *Proceedings of the IEEE/CVF Conference on Computer Vision and Pattern Recognition*, pages 4389–4398, 2024.
- [45] Jinbo Yan, Rui Peng, Zhiyan Wang, Luyang Tang, Jiayu Yang, Jie Liang, Jiahao Wu, and Ronggang Wang. Instant gaussian stream: Fast and generalizable streaming of dynamic scene reconstruction via gaussian splatting. *arXiv preprint arXiv:2503.16979*, 2025.
- [46] Taoran Yi, Jiemin Fang, Junjie Wang, Guanjun Wu, Lingxi Xie, Xiaopeng Zhang, Wenyu Liu, Qi Tian, and Xinggang Wang. Gaussiandreamer: Fast generation from text to 3d gaussians by bridging 2d and 3d diffusion models. In *Proceedings of the IEEE/CVF Conference on Computer Vision and Pattern Recognition*, pages 6796–6807, 2024.
- [47] Ye Yuan, Xueting Li, Yangyi Huang, Shalini De Mello, Koki Nagano, Jan Kautz, and Umar Iqbal. Gavatar: Animatable 3d gaussian avatars with implicit mesh learning. In *Proceedings of the IEEE/CVF Conference on Computer Vision and Pattern Recognition*, pages 896–905, 2024.

- [48] Yu-Ting Zhan, Cheng-Yuan Ho, Hebi Yang, Yi-Hsin Chen, Jui Chiu Chiang, Yu-Lun Liu, and Wen-Hsiao Peng. Cat-3dgs: A context-adaptive triplane approach to rate-distortion-optimized 3dgs compression. *arXiv preprint arXiv:2503.00357*, 2025.
- [49] Kai Zhang, Sai Bi, Hao Tan, Yuanbo Xiangli, Nanxuan Zhao, Kalyan Sunkavalli, and Zexiang Xu. Gs-irm: Large reconstruction model for 3d gaussian splatting. In *European Conference on Computer Vision*, pages 1–19. Springer, 2024.
- [50] Richard Zhang, Phillip Isola, Alexei A Efros, Eli Shechtman, and Oliver Wang. The unreasonable effectiveness of deep features as a perceptual metric. In *Proceedings of the IEEE conference on computer vision and pattern recognition*, pages 586–595, 2018.
- [51] Xuanyu Zhang, Jiarui Meng, Runyi Li, Zhipei Xu, Jian Zhang, et al. Gs-hider: Hiding messages into 3d gaussian splatting. *Advances in Neural Information Processing Systems*, 37:49780–49805, 2025.
- [52] Xuanyu Zhang, Jiarui Meng, Zhipei Xu, Shuzhou Yang, Yanmin Wu, Ronggang Wang, and Jian Zhang. Securegs: Boosting the security and fidelity of 3d gaussian splatting steganography. *arXiv preprint arXiv:2503.06118*, 2025.
- [53] Yushu Zhang, Jiahao Zhu, Mingfu Xue, Xinpeng Zhang, and Xiaochun Cao. Adaptive 3d mesh steganography based on feature-preserving distortion. *IEEE Transactions on Visualization and Computer Graphics*, 2023.
- [54] Junsheng Zhou, Weiqi Zhang, and Yu-Shen Liu. Diffgs: Functional gaussian splatting diffusion. *Advances in Neural Information Processing Systems*, 37:37535–37560, 2024.
- [55] Jiahao Zhu, Yushu Zhang, Xinpeng Zhang, and Xiaochun Cao. Gaussian model for 3d mesh steganography. *IEEE Signal Processing Letters*, PP:1–1, 08 2021.
- [56] Jiren Zhu, Russell Kaplan, Justin Johnson, and Li Fei-Fei. Hidden: Hiding data with deep networks. In *Proceedings of the European conference on computer vision (ECCV)*, pages 657–672, 2018.
- [57] Ruijie Zhu, Yanzhe Liang, Hanzhi Chang, Jiacheng Deng, Jiahao Lu, Wenfei Yang, Tianzhu Zhang, and Yongdong Zhang. Motions: Exploring explicit motion guidance for deformable 3d gaussian splatting. *Advances in Neural Information Processing Systems*, 37:101790–101817, 2025.

## Appendix

### A Broader impacts

Our proposed CompMarkGS is an invisible watermarking method for 3D assets, such as 3D Gaussian Splatting (3DGS), which remains recoverable even after aggressive compression. Our work has three key social impacts:

- **Security:** CompMarkGS enables copyright protection of 3D assets distributed across diverse digital environments without compromising visual quality. This capability supports copyright protection and sustainable revenue generation across a wide range of 3D content creators.
- **Applicability:** CompMarkGS ensures watermark robustness under high-ratio compression, enabling protected 3DGS to be reliably utilized on resource-constrained devices, such as mobile phones and head-mounted displays. These protected 3DGS can be safely deployed in virtual reality (VR), augmented reality (AR), medical imaging, and other 3D applications without compromising watermark integrity.
- **Sustainability:** To the best of our knowledge, CompMarkGS is the first watermarking method to achieve watermark robustness against compression. Building on this work, it will provide a foundation for other researchers and practitioners to extend the approach, contributing to the advancement of watermarking research across a variety of compression formats.

### B More implementation details

#### B.1 Details of training

Our proposed CompMarkGS trains the anchor-based 3DGS from scratch with the watermark, in contrast to existing methods [13, 14, 15] that rely on fine-tuning pre-trained 3DGS models. We train CompMarkGS for 30,000 iterations. Anchor growing is performed between 1,600 and 15,000 iterations, first using conventional anchor growing and then switching to the proposed frequency-aware anchor growing strategy for fine-grained refinement. The loss function for watermark training consists of the original anchor-based 3DGS [25] loss  $\mathcal{L}_{\text{scaffold}}$  and three additional components: HSV loss  $\mathcal{L}_{\text{hsv}}$ , frequency loss  $\mathcal{L}_{\text{freq}}$ , and message loss  $\mathcal{L}_{\text{msg}}$ . Before watermark training begins, we pre-train a HiDDeN [56] message decoder on the MS-COCO dataset [24] for 32, 48, and 64-bit messages following the strategy from 3D-GSW [15] and Stable Signature [10]. During the subsequent watermark training, the pre-trained decoder is kept fixed. Additionally, the compression ratio of the compression method used in all experiments is set to 0.004.

#### B.2 Details of high-pass filter

Early digital watermarking studies hide the watermark in the high-frequency bands of an image to keep it imperceptible. However, the watermark embedded in high-frequency regions is vulnerable to image distortions such as JPEG compression. More recent work, therefore, embeds the watermark in the low-frequency bands, which are more robust to such attacks. The drawback is that low-frequency components represent essential information, including the global structure and color distribution of the image. Modifying these components can degrade visual coherence and affect the perception of fine details such as edges and textures.

The conventional anchor growing strategy computes the mean gradient of the Gaussians within each voxel and places a new anchor point only if no anchor already exists in voxels whose mean gradient exceeds a threshold. During anchor-based 3DGS training, voxels with high mean gradients are primarily associated with regions that form the coarse structure of the scene. As a result, densification rarely occurs in fine-detail areas, and when a watermark is embedded, those under-represented regions are more susceptible to quality degradation.

To address this limitation, we propose a frequency-aware anchor growing strategy that selectively densifies Gaussians located in high-frequency regions. Specifically, we apply a Discrete Fourier Transform (DFT) to convert the rendered image into the frequency domain. To isolate high-frequency components, we use a high-pass filter mask  $M_h$  that emphasizes high-frequency regions while

suppressing low-frequency ones in the frequency domain:

$$M_h(p) = 1 - \exp\left(-\frac{(d(p) - \tau)^2}{2\beta}\right), \quad (11)$$

where  $d(p)$  denotes the Euclidean distance between a pixel  $p$  and the center of the image.  $\tau$  defines the cutoff threshold of the mask and  $\beta$  determines the degree of attenuation. The resulting mask  $M_h$  is multiplied element-wise with the Fourier-transformed image to suppress low-frequency components and preserve only the high-frequency details. Afterward, we apply the Inverse Discrete Fourier Transform (IDFT) to reconstruct the filtered images in the spatial domain, resulting in the high-frequency rendered images  $I'_{hf}$  and the high-frequency ground truth images  $I_{hf}$ . Further details of the frequency-aware anchor growing process can be found in the main paper. (See main paper Sec.4.3)

### B.3 Details of frequency-aware anchor growing

We propose a frequency-aware anchor growing strategy that efficiently identifies and densifies Gaussians in high-frequency regions to mitigate visual quality degradation caused by watermark embedding. Specifically, we first compute a pixel-wise SSIM-based error map  $P_{error}$  (See main paper Sec.4.3) between the high-frequency rendered image  $I'_{hf}$  and the ground truth image  $I_{hf}$ , both extracted in the frequency domain. (B.2) This error map  $P_{error}$  highlights pixel regions where high-frequency information is not faithfully reconstructed. To identify pixel regions that contain visually important fine details, we compute the median value  $\tilde{P}_{error}$  of the SSIM-based pixel-wise error map  $P_{error}$ . Using the median value  $\tilde{P}_{error}$  ensures a more meaningful identification of high-frequency regions by mitigating the influence of outlier pixels, which may otherwise dominate when relying on the maximum value of the SSIM-based pixel-wise error map  $P_{error}$ . We then generate a binary mask  $I_{mask}$  by filtering pixels whose error values fall within the interval  $[\tilde{P}_{error} - \epsilon, \tilde{P}_{error} + \epsilon]$ :

$$I_{mask}(p) = \begin{cases} 1, & \text{if } |P_{error}(p) - \tilde{P}_{error}| \leq \epsilon, \\ 0, & \text{otherwise} \end{cases}, \quad (12)$$

where  $p$  denotes the pixel coordinates in the image. Subsequently, we construct a binary mask  $G_{mask}$  to select the 3D Gaussian points that 2D projections fall within the boundaries of the image:

$$G_{mask}(k) = \begin{cases} 1, & \text{if } 0 \leq x < W \quad \text{and} \quad 0 \leq y < H, \\ 0, & \text{otherwise} \end{cases}, \quad (13)$$

where  $k = (x, y)$  denotes the pixel coordinates of the 2D Gaussian, and  $W$  and  $H$  represent the width and height of the image, respectively. Using the two binary masks  $I_{mask}$  and  $G_{mask}$ , we generate a boolean mask  $F_{mask}$  that identifies Gaussians located in specific high-frequency regions by matching their 2D coordinates to the high-frequency pixel locations:

$$F_{mask}(k) = I_{mask}(k) \cdot G_{mask}(k), \quad (14)$$

where  $k$  denotes the pixel coordinates of the 2D Gaussian. During the anchor growing process, we calculate the average of Gaussians within the voxel regions selected by the computed boolean mask  $F_{mask}$ , based on the accumulated sum of their gradients. If the average gradient exceeds the threshold  $\tau_{high}^g = 0.00015$  and no anchor exists in the corresponding voxel, a new anchor is added. The threshold for the accumulated opacity used in the subsequent anchor pruning step is set to  $\tau_{high}^o = 0.15$ .

### B.4 Details of HSV loss

In the field of digital watermarking, achieving imperceptible watermark embedding is a primary research goal. However, there exists an inherent trade-off between invisibility and bit accuracy. When training a model to embed a watermark in 3D Gaussian Splatting (3DGS), color artifacts emerge due to the tendency to embed the watermark into specific Gaussians to achieve high bit accuracy. Additionally, these artifacts occur particularly in regions rendered by a small number of Gaussians, where even slight modifications to the Gaussians can lead to noticeable distortions.

Although the RGB color space is widely used for image representation, prior work on image sharpening [17] indicates that the RGB color space does not fully account for the perceptual characteristics

of the human visual system. In particular, the human visual system is more sensitive to luminance variations than to chromatic changes [11]. Unlike the RGB color space, the Hue, Saturation, and Value (HSV) space separates chromatic information (Hue and Saturation) from luminance (Value), enabling more precise detection and suppression of color artifacts. Based on this property, we introduce an HSV loss that enhances rendering quality while preserving high bit accuracy.

To isolate specific regions in the HSV space, we construct binary masks (See main paper Eq.7) by filtering pixels based on predefined hue ranges  $H_c$ , along with threshold conditions on saturation  $\tau_c^s$  and value  $\tau_c^v$ , corresponding to color  $c \in \mathcal{C}$ , where  $\mathcal{C} = \{R, G, B\}$ . Each pixel  $p \in \Omega$ , where  $\Omega \subset \mathbb{R}^2$  denotes the spatial domain of the image, is evaluated based on its HSV values. Let  $S(p) \in [0, 1]$  and  $V(p) \in [0, 1]$  denote the saturation and value components at pixel  $p$ , respectively. We define the hue range  $H_c$  for each color as follows:

$$\begin{aligned} H_R &\in \left[0, \frac{\pi}{3}\right) \cup \left[\frac{5\pi}{6}, 2\pi\right), \text{ if } S(p) \geq \tau_R^s \text{ and } V(p) \geq \tau_R^v, \\ H_G &\in \left[\frac{\pi}{3}, \pi\right), \text{ if } S(p) \geq \tau_G^s \text{ and } V(p) \geq \tau_G^v, \\ H_B &\in \left[\pi, \frac{5\pi}{3}\right), \text{ if } S(p) \geq \tau_B^s \text{ and } V(p) \geq \tau_B^v, \end{aligned} \quad (15)$$

where  $H(p) \in [0, 2\pi)$  denotes the hue value at pixel  $p$ . Pixels that do not satisfy the corresponding saturation or value thresholds are excluded from the mask, even if their hue lies within the specified range. We set thresholds for the red with  $\tau_R^s = 0.4$  and  $\tau_R^v = 0$ , while using relaxed thresholds  $\tau_c^s = 0.2, \tau_c^v = 0.2$  for the green and blue.

## C Computing resources

We evaluate the rendering performance of our method and baselines [13, 14, 15] by measuring FPS. As shown in Tab.7, our method exceeds the real-time rendering threshold of 30 FPS across the Blender [29], LLFF [28], and Mip-NeRF 360 [3] datasets. These results demonstrate the practical applicability and rendering efficiency of our proposed CompMarkGS.

Table 7: FPS results for each of the Blender, LLFF, and Mip-NeRF 360 datasets. Based on 48-bit messages, results are averaged with both HAC and ContextGS after compression.

Methods	FPS↑		
	Blender	LLFF	Mip-NeRF 360
WateRF [14]	199.30	19.31	41.98
GaussianMarker [13]	166.45	16.24	28.54
3D-GSW [15]	220.60	22.67	50.64
CompMarkGS	<b>230.39</b>	<b>35.30</b>	<b>67.58</b>

## D Additional results

### D.1 Embedding the watermark in anchor attributes

We evaluate the impact of embedding the watermark into different anchor attributes (position, scaling, offsets) by measuring the rendering quality and bit accuracy. As discussed in the main paper (See main paper Sec.4.1), the proposed watermark embedding feature is adjusted to match the dimensionality of each anchor attribute to ensure compatibility during insertion. As reported in Tab. 8, embedding the watermark into attributes other than the anchor feature results in a noticeable degradation in rendering quality. Unlike the anchor feature, which predicts Gaussian attributes via individual MLPs, position and scaling directly affect the position and shape of each Gaussian. Consequently, embedding into these attributes causes significant degradation in both rendering quality and bit accuracy. Offsets, which represent the relative position of Gaussians from anchor points within each voxel, yield better bit accuracy than position and scaling but still suffer from lower visual quality. These results confirm that the proposed method can reliably embed the watermark into the model without compromising the scene fidelity.

Table 8: Ablation studies on watermark embedding into different anchor attributes. Results are reported for 48-bit messages and averaged over three datasets using ContextGS after compression.

Target Parameter	Bit Acc(%) $\uparrow$	PSNR $\uparrow$	SSIM $\uparrow$	LPIPS $\downarrow$
Position	82.37	18.49	0.632	0.432
Scaling	64.68	13.40	0.466	0.474
Offsets	93.98	25.32	0.755	0.322
Anchor Feature (Ours)	94.03	27.55	0.844	0.173

## D.2 Effectiveness of our contributions

To evaluate the individual contribution of each component, we conduct ablation studies by selectively removing the frequency-aware anchor growing (FAG), quantization distortion layer (QDL), and HSV loss  $\mathcal{L}_{hsv}$  from our proposed method. We perform under HAC [7] and ContextGS [39] compression settings, and we compare the resulting bit accuracy and rendering quality. As shown in Tab. 9, removing QDL causes a notable decrease in bit accuracy, demonstrating its effectiveness in preserving watermark information embedded in anchor attributes under quantization-based compression. In contrast, removing FAG maintains high bit accuracy but leads to degraded rendering quality. This highlights the role of FAG in enhancing visual fidelity by promoting anchor densification in high-frequency regions. Removing the HSV loss also results in a slight degradation in rendering quality, particularly in LPIPS. These results indicate its effectiveness in suppressing color artifacts that are not adequately addressed by RGB-based losses alone. Notably, we observe that removing all components results in the most significant performance degradation. These findings collectively demonstrate that FAG, QDL, and HSV loss each contribute critically to balancing bit accuracy and rendering quality under compression. The integration of all three components yields the best overall performance in compressed settings.

Table 9: Ablation studies on frequency-aware anchor growing (FAG), quantization distortion layer (QDL), and HSV loss  $\mathcal{L}_{hsv}$ . Results are reported for 48-bit messages and averaged over three datasets under HAC and ContextGS after compression.

FAG	QDL	$\mathcal{L}_{hsv}$	HAC+CompMarkGS				ContextGS+CompMarkGS			
			Bit Acc(%) $\uparrow$	PSNR $\uparrow$	SSIM $\uparrow$	LPIPS $\downarrow$	Bit Acc(%) $\uparrow$	PSNR $\uparrow$	SSIM $\uparrow$	LPIPS $\downarrow$
–	–	–	90.67	26.44	0.827	0.196	87.63	25.56	0.812	0.223
–	✓	✓	93.95	27.54	0.849	0.178	90.35	27.15	0.841	0.198
✓	–	✓	90.75	26.75	0.844	0.182	88.09	25.04	0.801	0.229
✓	✓	–	92.57	27.49	0.852	0.179	90.23	27.19	0.841	0.200
✓	✓	✓	95.92	27.65	0.852	0.177	94.03	27.55	0.844	0.173

## D.3 Effectiveness of HSV loss

When only RGB-based loss functions are used for watermark embedding, the optimization of 3DGS fails to consider the characteristics of the human visual system. As a result, 3DGS with a watermark renders color artifacts in the rendered images, particularly in regions with strong chromatic and luminance variations. These artifacts are observed in Fig.6 and Fig.7, despite achieving high bit accuracy.

To address this, we introduce an HSV loss that aligns more closely with the perceptual characteristics of the human visual system. HSV color space separates chromatic components (Hue and Saturation) from luminance (Value), making it more suitable for detecting and reducing color artifacts. As shown in Fig. 6, binary masks of HSV loss successfully detect color artifacts in each color channel. Moreover, Fig. 7 shows that HSV loss allows 3DGS to focus its optimization on minimizing color artifacts, maintaining high bit accuracy. These results show that HSV loss effectively reduces color artifacts while preserving high bit accuracy and rendering quality.

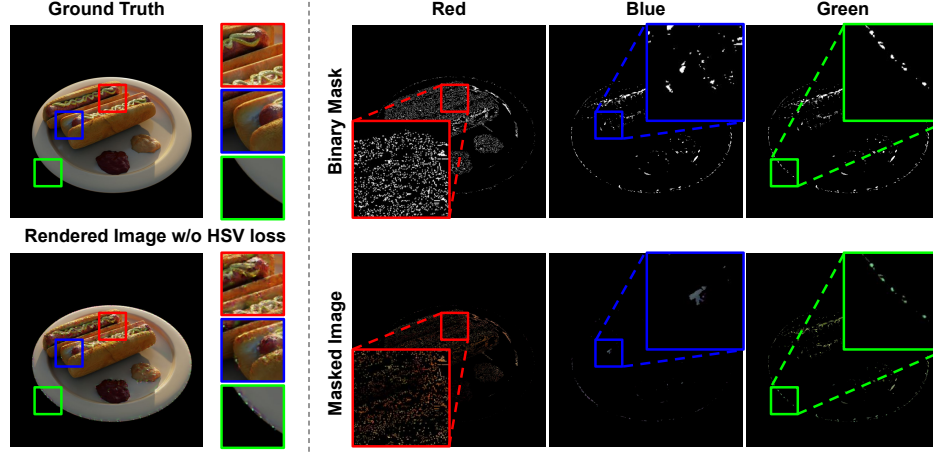


Figure 6: Visualization of the binary mask and masked image for each color channel (Red, Green, and Blue). The left column shows the ground truth and the rendered image without HSV loss. The right columns present the binary masks (top) and masked results (bottom) for each color channel. This result is based on 48-bit messages.

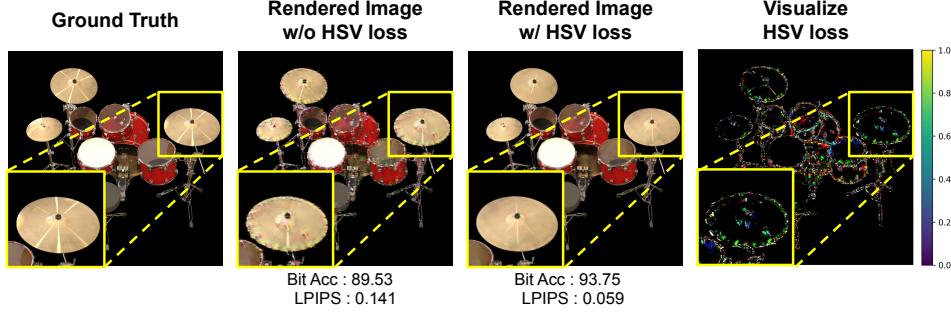


Figure 7: Visualization of HSV loss. The comparison is performed between images rendered with and without the HSV loss. This result is based on 48-bit messages.

#### D.4 Robustness to model distortion comparison

Fig.8 and Fig.9 show the bit accuracy under different levels of model distortion. We conduct three model distortions: 1) adding Gaussian noise to all model parameters, 2) randomly removing anchors, and 3) randomly cloning anchors. Across different distortion strengths, our proposed method consistently outperforms the baseline. Notably, under prune and clone distortion settings, our method exhibits less performance degradation, owing to the incorporation of both pruning and anchor growing during training in CompMarkGS. These results demonstrate that our method achieves superior performance over the baseline, even under severe model distortions.

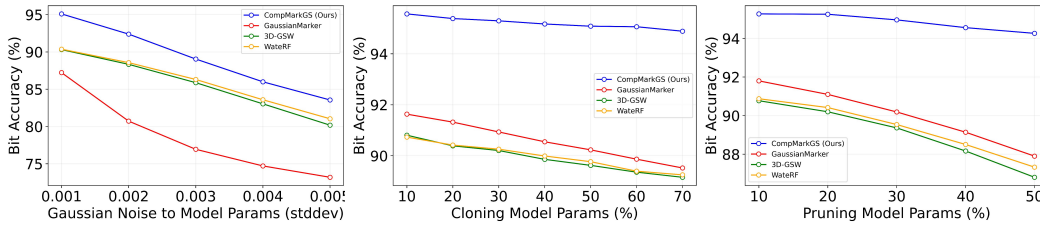


Figure 8: Comparison of the baselines and our method under various model distortions and distortion strengths. We conduct three model distortions: 1) Gaussian noise, 2) cloning anchors, and 3) pruning anchors. The blue line represents the results of our method. Results represent the average score across Blender, LLFF, and Mip-NeRF 360 datasets using 48-bit messages. All baselines were tested within an anchor-based 3DGS framework, employing HAC.



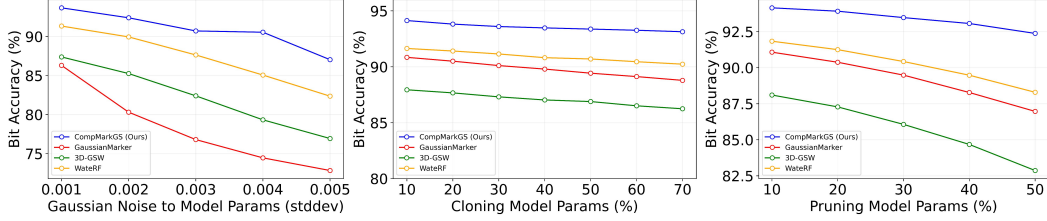


Figure 9: Comparison of the baselines and our method under various model distortions and distortion strengths. We conduct three model distortions: 1) Gaussian noise, 2) cloning anchors, and 3) pruning anchors. The blue line represents the results of our method. Results represent the average score across Blender, LLFF, and Mip-NeRF 360 datasets using 48-bit messages. All baselines were tested within an anchor-based 3DGS framework, employing ContextGS.

## D.5 Performance across compression levels

Compression plays a crucial role in determining the trade-off between model size and performance in terms of bit accuracy and rendering quality. Fig. 10 shows the relationship among model size, bit accuracy, and rendering quality under two different compression schemes: HAC [7] and ContextGS [39]. Fig. 10 indicates that a lower compression level leads to better bit accuracy and rendering quality. Our method consistently outperforms other methods, achieving the highest bit accuracy and rendering quality across varying model sizes. Notably, for HAC compression, we achieve bit accuracy of 90% with model size less than 10 MB, while other methods only reach 60% under the same model size. These results highlight the effectiveness and robustness of CompMarkGS.

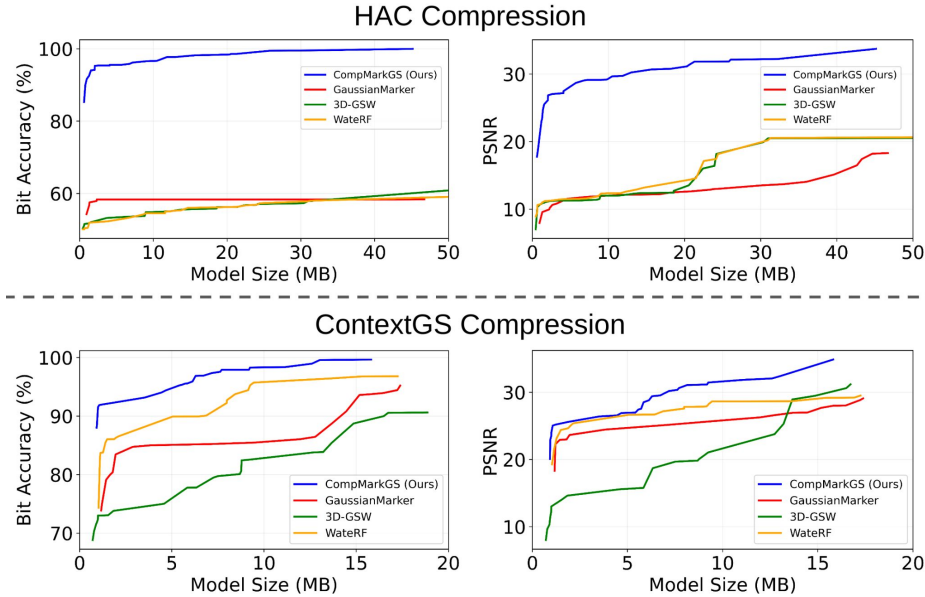


Figure 10: Performance of bit accuracy and rendering quality under different compression levels. A larger model size corresponds to a lower compression level. The blue line represents the results of our method. Results represent the average score across Blender, LLFF, and Mip-NeRF 360 datasets using 48-bit messages.

## D.6 Additional qualitative results

Fig. 11 through Fig. 19 visualize all results rendered after compression using our method with HAC and ContextGS, along with the difference ( $\times 5$ ) between the original images and the watermarked images.

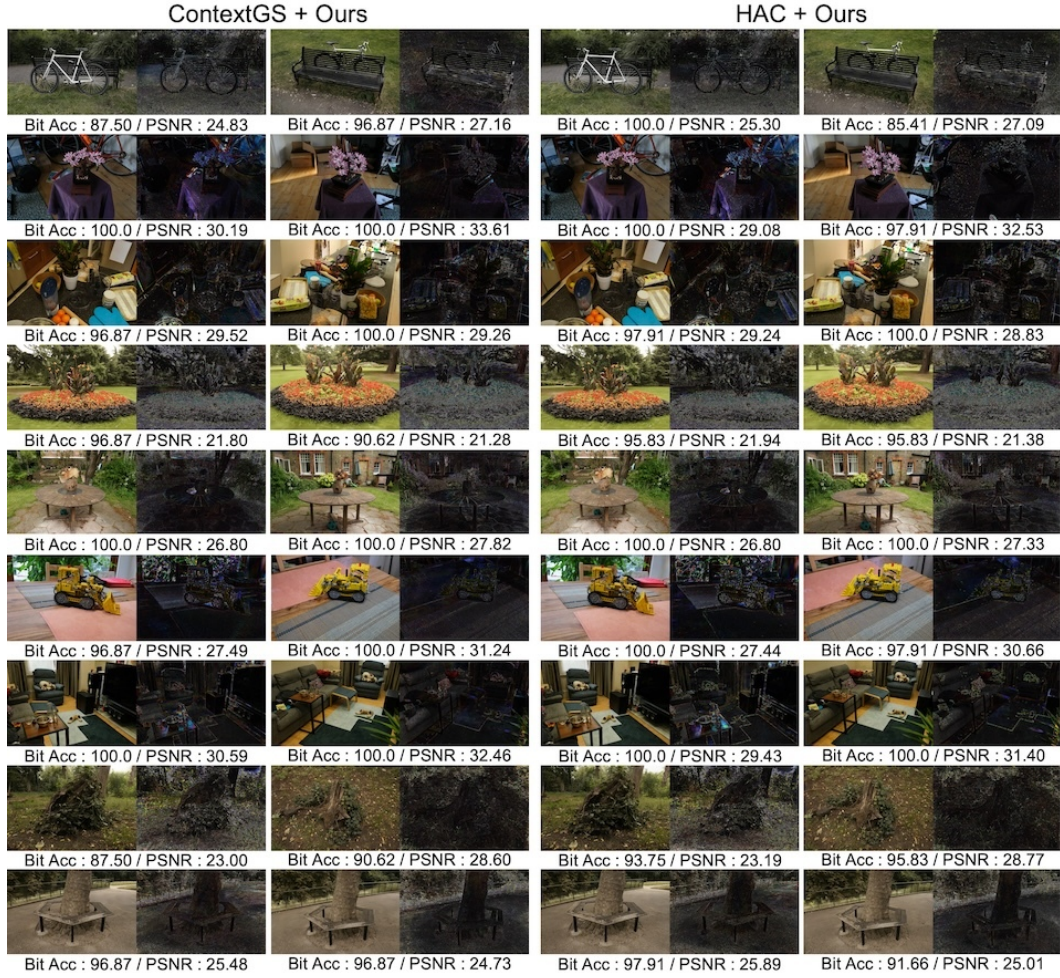


Figure 11: Rendering quality of various rendering outputs generated by our method on the Mip-NeRF 360 dataset. We show the differences ( $\times 5$ ). The closer it is to white, the greater the discrepancy between the ground truth and the rendered image. The results were obtained using 32-bit messages after compression.



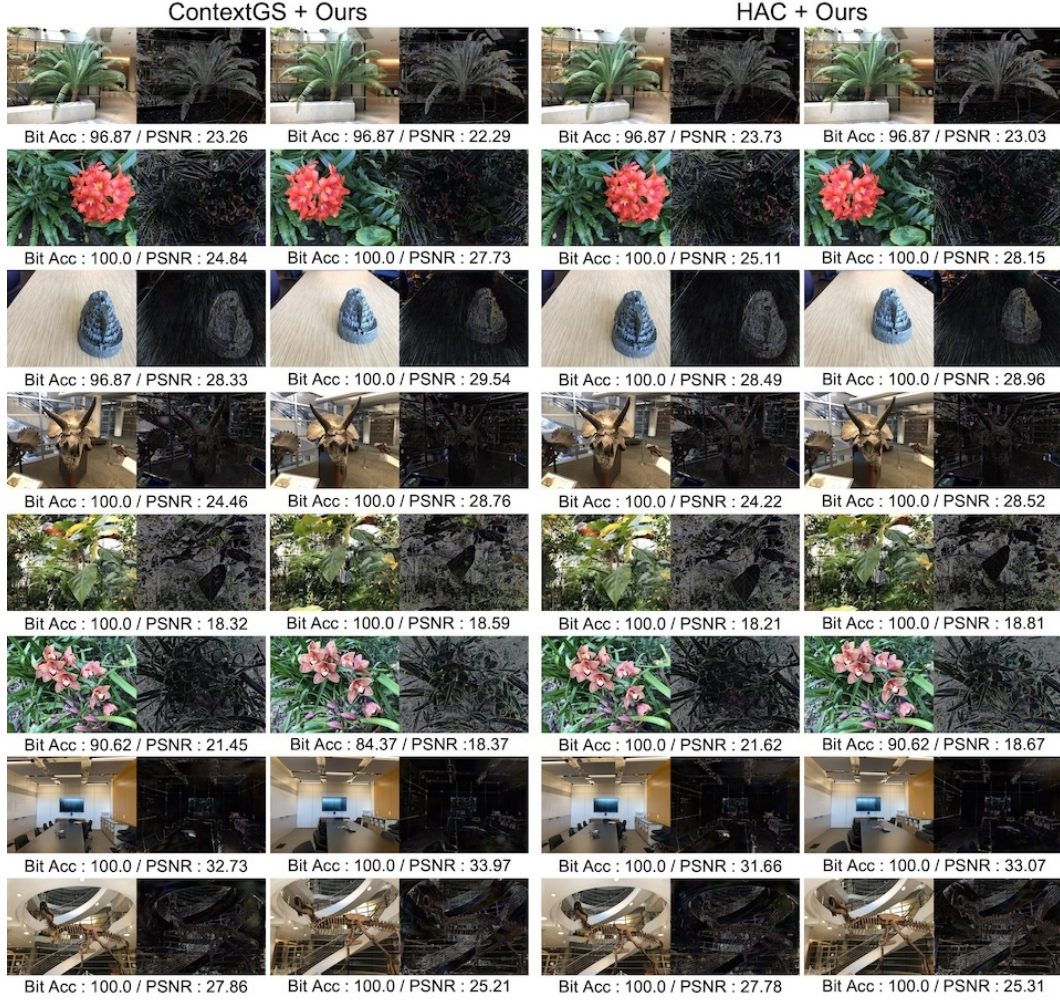


Figure 12: Rendering quality of various rendering outputs generated by our method on the LLFF dataset. We show the differences ( $\times 5$ ). The closer it is to white, the greater the discrepancy between the ground truth and the rendered image. The results were obtained using 32-bit messages after compression.

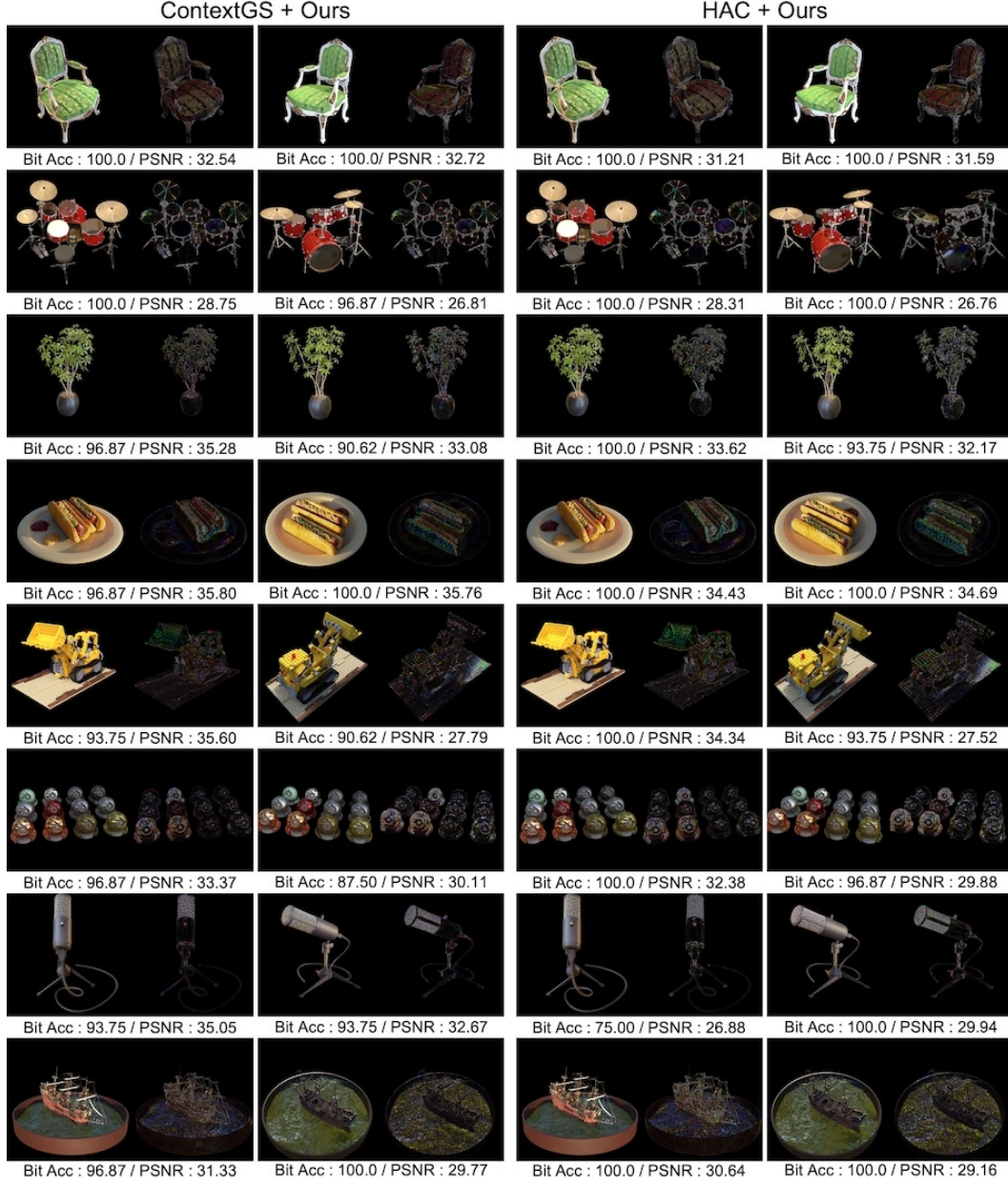


Figure 13: Rendering quality of various rendering outputs generated by our method on the Blender dataset. We show the differences ( $\times 5$ ). The closer it is to white, the greater the discrepancy between the ground truth and the rendered image. The results were obtained using 32-bit messages after compression.



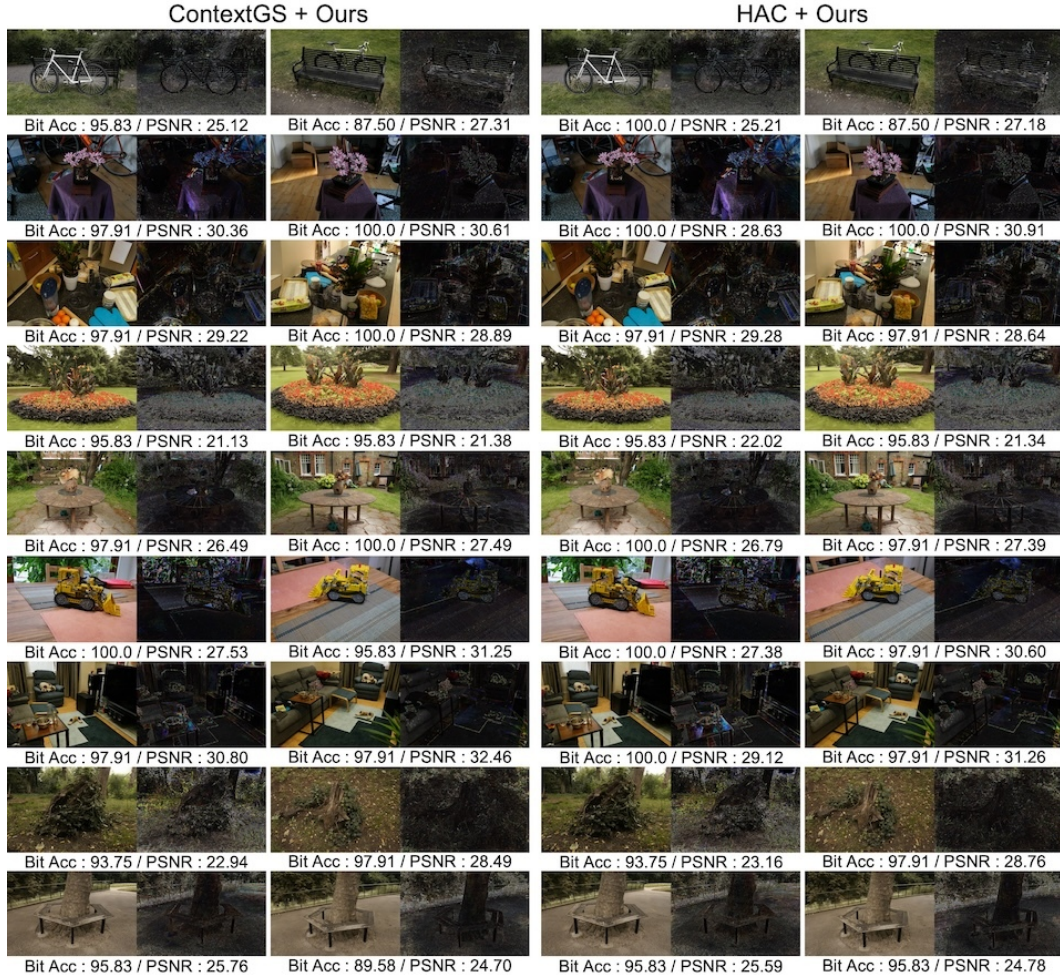


Figure 14: Rendering quality of various rendering outputs generated by our method on the Mip-NeRF 360 dataset. We show the differences ( $\times 5$ ). The closer it is to white, the greater the discrepancy between the ground truth and the rendered image. The results were obtained using 48-bit messages after compression.

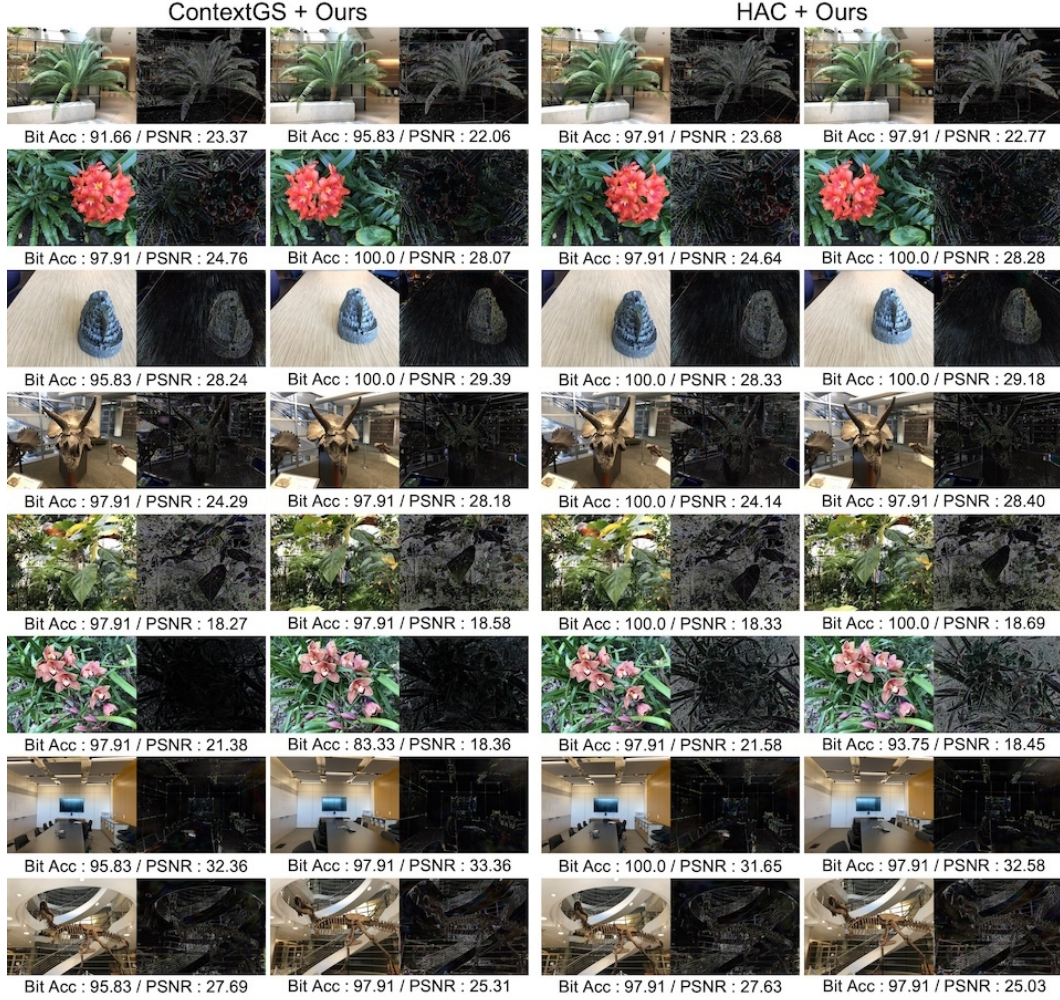


Figure 15: Rendering quality of various rendering outputs generated by our method on the LLFF dataset. We show the differences ( $\times 5$ ). The closer it is to white, the greater the discrepancy between the ground truth and the rendered image. The results were obtained using 48-bit messages after compression.



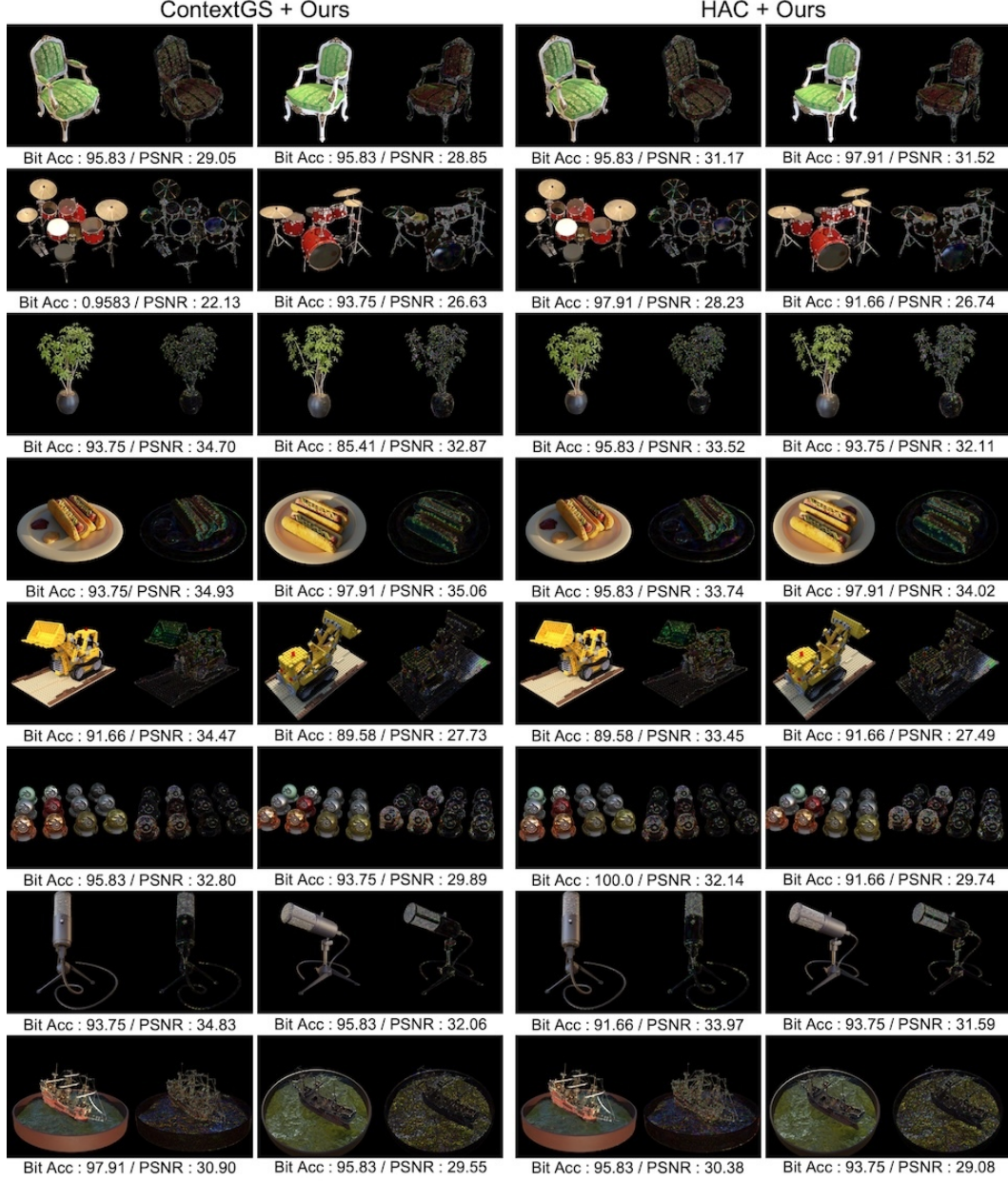


Figure 16: Rendering quality of various rendering outputs generated by our method on the Blender dataset. We show the differences ( $\times 5$ ). The closer it is to white, the greater the discrepancy between the ground truth and the rendered image. The results were obtained using 48-bit messages after compression.



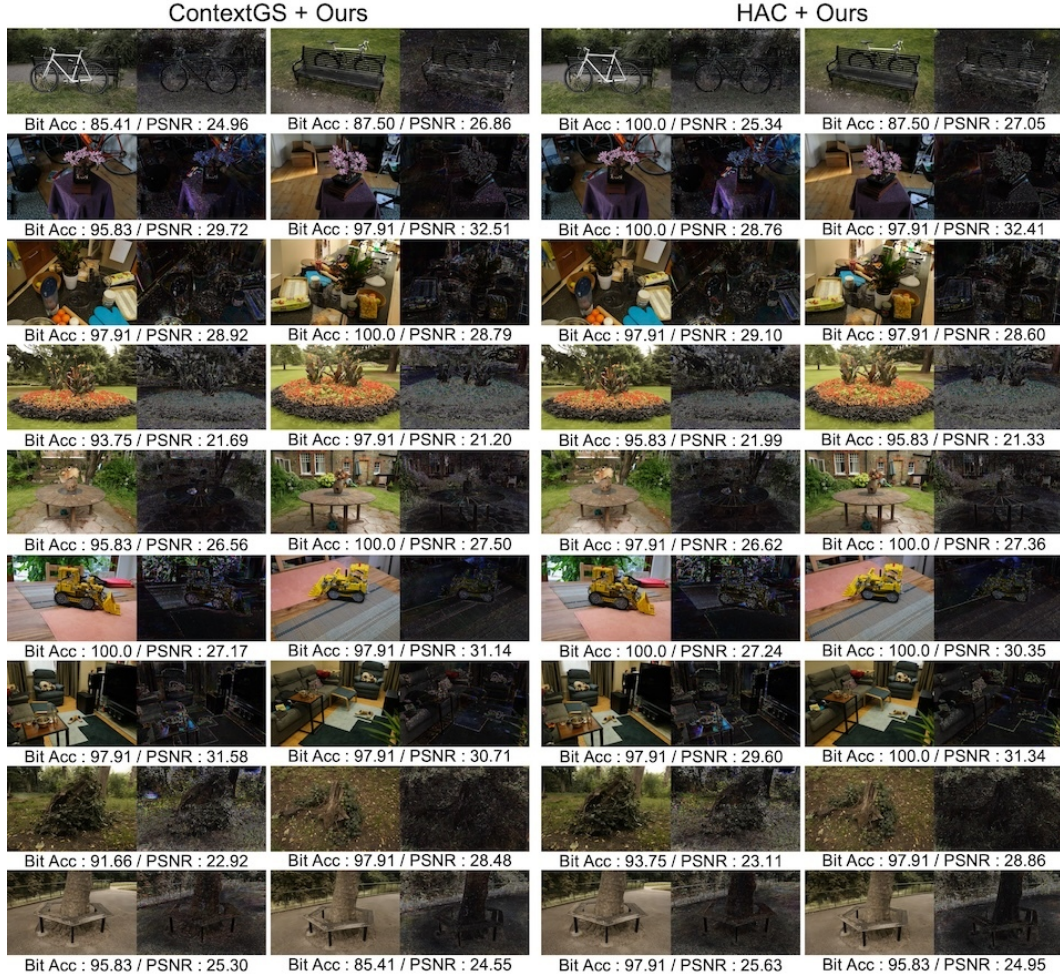


Figure 17: Rendering quality of various rendering outputs generated by our method on the Mip-NeRF 360 dataset. We show the differences ( $\times 5$ ). The closer it is to white, the greater the discrepancy between the ground truth and the rendered image. The results were obtained using 64-bit messages after compression.

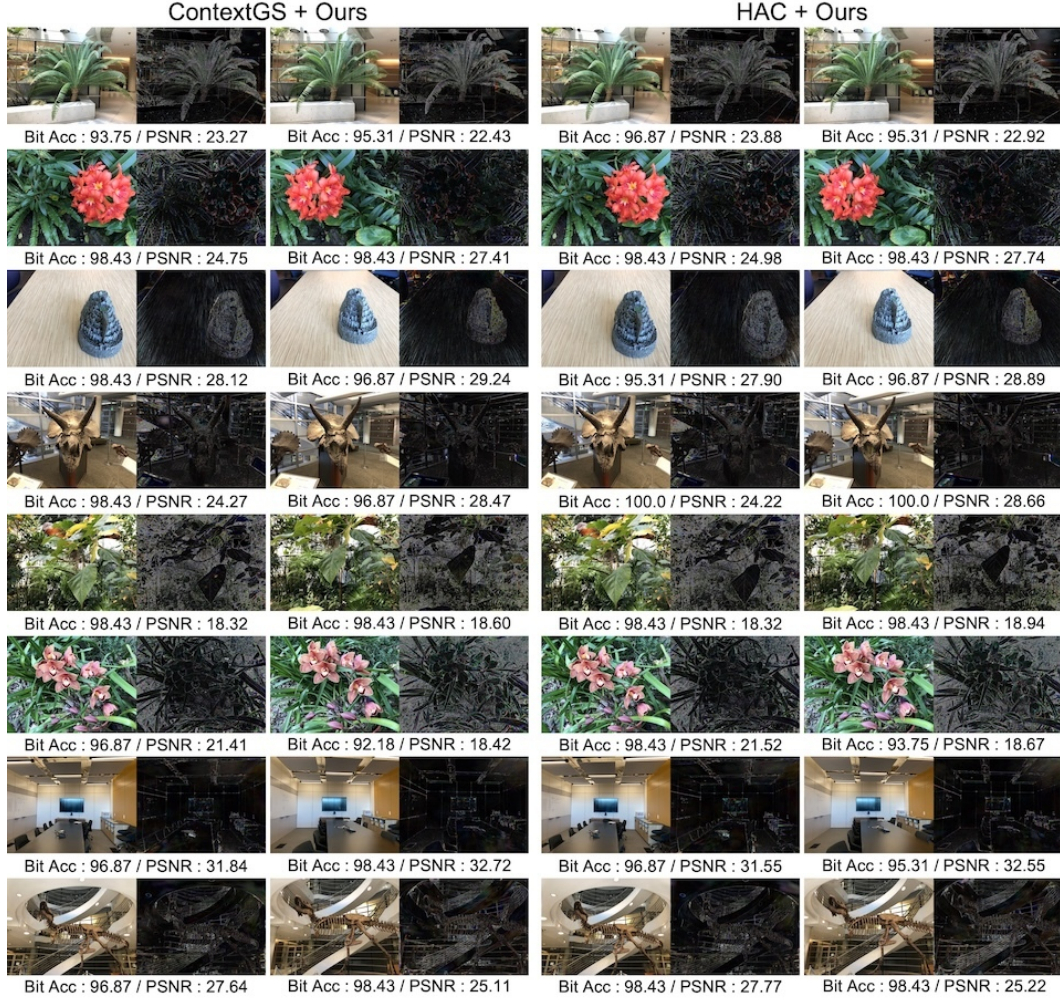


Figure 18: Rendering quality of various rendering outputs generated by our method on the LLFF dataset. We show the differences ( $\times 5$ ). The closer it is to white, the greater the discrepancy between the ground truth and the rendered image. The results were obtained using 64-bit messages after compression.



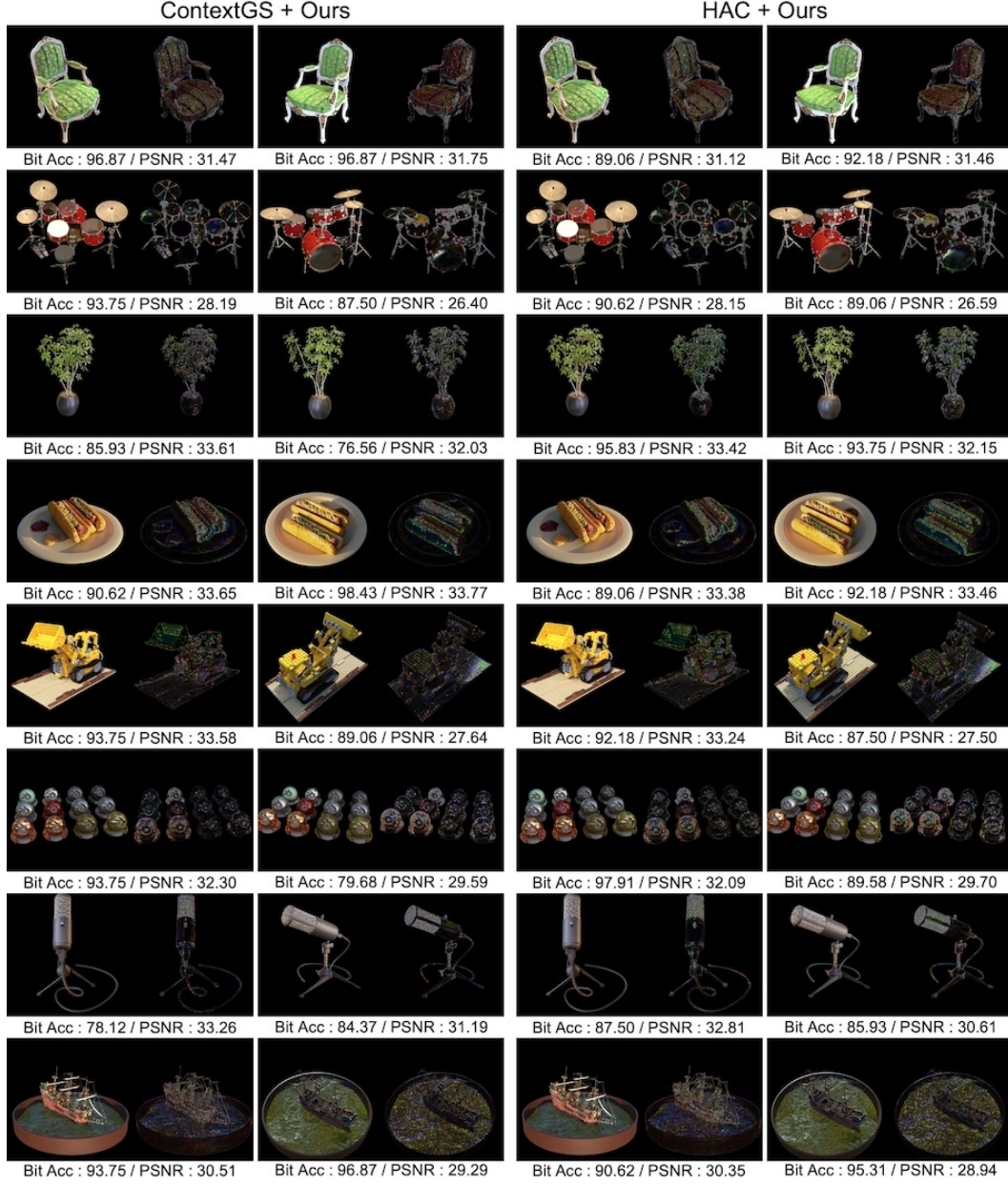


Figure 19: Rendering quality of various rendering outputs generated by our method on the Blender dataset. We show the differences ( $\times 5$ ). The closer it is to white, the greater the discrepancy between the ground truth and the rendered image. The results were obtained using 64-bit messages after compression.